

# Closed-Form Feedback-Free Learning with Forward Projection

Robert O’Shea<sup>1\*</sup> and Bipin Rajendran<sup>1\*</sup>

<sup>1\*</sup>Centre for Intelligent Information Processing Systems, Department of Engineering, King’s College London, Strand, London, WC2R 2LS, London, UK.

\*Corresponding author(s). E-mail(s): [k1930297@kcl.ac.uk](mailto:k1930297@kcl.ac.uk);  
[bipin.rajendran@kcl.ac.uk](mailto:bipin.rajendran@kcl.ac.uk);

## Abstract

State-of-the-art methods for backpropagation-free learning employ local error feedback to direct iterative optimisation via gradient descent. In this study, we examine the more restrictive setting where retrograde communication from neuronal outputs is unavailable for pre-synaptic weight optimisation. To address this challenge, we propose **Forward Projection** (FP). This novel randomised closed-form training method requires only a single forward pass over the entire dataset for model fitting, without retrograde communication. Our key innovation is generating target values for pre-activation membrane potentials at each layer via nonlinear projections of pre-synaptic inputs and the labels. Our approach generates target potentials from randomised encodings combining information from inputs and labels. Local loss functions are optimised over pre-synaptic inputs using closed-form regression, without feedback from neuronal outputs or downstream layers. Interpretability is a key advantage of FP training; membrane potentials of hidden neurons in FP-trained networks encode information which are interpretable layer-wise as label predictions. We demonstrate the effectiveness of FP across four biomedical datasets, comparing it with backpropagation and local learning techniques such as Forward-Forward training and Local Supervision in multi-layer perceptron and convolutional architectures. In some few-shot learning tasks, FP yielded more generalisable models than those optimised via backpropagation. In large-sample tasks, FP-based models achieve generalisation comparable to gradient descent-based local learning methods while requiring only a single forward propagation step, achieving significant speed up for training.

Interpretation functions defined on local neuronal activity in FP-based models successfully identified clinically salient features for diagnosis in two distinct datasets – identification of key signatures of myocardial infarction in time-series data from electrocardiogram sequences and detection of regions of choroid neovascularisation in optical coherence tomography images.

Forward Projection is a computationally efficient machine learning approach that yields interpretable neural network models without retrograde communication of neuronal activity during training.

**Keywords:** Forward learning, Neural networks, Local learning, Energy-efficient computing, Explainable Artificial Intelligence

## Introduction

A core task in neural network training is synaptic “credit assignment” for error in downstream layers [1–3]. Although backpropagation has been established as the standard approach to this problem, its biological plausibility has been questioned [3–5]. Backpropagation requires bidirectional synaptic communication, which is incompatible with the unidirectional transmission of neural action potentials [3]. Consequently, backpropagation would require either symmetric neural connectivity or a parallel retrograde network for error feedback to earlier layers [3, 6, 7]. The backward pass traverses layers in reverse order of activation, leading to temporal discordance between forward and backward operations and necessitating storage of hidden activations. Furthermore, gradient descent requires hidden neural activations to be differentiable throughout. To approximate backpropagation in a more biologically plausible way, approaches such as Predictive Coding [5, 8] and Difference Target Propagation [1] seek to align forward neural activity with a backward network that mirrors the forward architecture, effectively implementing an inverse model. Various strategies have been proposed to address the credit assignment problem with reduced retrograde communication requirements. Auxiliary loss functions computed on the activations of individual layers have been proposed to shorten the backward pass [9–11]. A prominent example is the layer-wise greedy optimisation method that aims to minimise the costs of backpropagation applying locally supervised (LS) at each layer [9, 12]. Extensions of this approach include deep continuous local learning [10] and single layer updating [13]. Hebbian learning rules using asymmetric feedback weights have been explored, allowing for independent updates for forward and feedback pathways [14].

Recent approaches have also explored using two forward passes to facilitate communication between upstream and downstream neurons [15–18]. The “Forward-Forward” (FF) learning algorithm [15], is an approach in which data and label hypotheses are combined as inputs, with optimisation seeking to upregulate neural response to correctly labelled inputs and subdue responses to spuriously labelled inputs. However, inference under the original forward learning algorithm requires a forward pass for

each hypothesised label, presenting issues for tasks with large label spaces [18]. The “PEPITA” algorithm proposed a preliminary forward pass to predict a label, which is used to generate spurious data-label instances for training [16].

The central issue with local learning methods in deep neural networks is that the optimal activity of hidden neurons is unknown during training, preventing direct observation of local error. Pre-defining activity targets for hidden neurons allows for heuristic local optimization. However, target definition strategies are a topic of ongoing research [19]. Techniques such as local-representation alignment and target propagation introduce target values for hidden activations using limited retrograde communication from downstream neurons [1, 11, 19–21]. Alternatively, target activities can be set as fixed random label projections computed during the forward pass, thereby permitting direct measurement of the error during the forward pass [11]. However, this approach may lead to highly correlated neuronal activity – a problem known as informational collapse [12]. Although additive noise permits maximal decorrelation of target potentials [1], it is uninformative with respect to the label, potentially impeding model fitting. Approaches such as random neural network features [22] forgo optimisation of hidden nodes entirely, projecting inputs to a random high-dimensional non-linear feature space. However, random feature layers require exponential scaling with respect to the input dimension to support downstream learning [23].

The “Predictive Coding” paradigm provides an insightful perspective on the collective functionality of intermediate neurons, proposing that local neural learning processes optimise the prediction of pre-synaptic neural inputs, minimising the “surprise” of out-of-distribution stimuli [5]. Approaches such as the “Difference Target Propagation” [1] reframe network layers as a series of autoencoders, where intermediate activations represent a series of encodings, transitioning from input information to label information. The issue of informational collapse in locally supervised SGD-trained models has been addressed by optimising the retention of information on the pre-synaptic activity [12]. “Prospective configuration” of target activities reformulates learning under the presumption that idealised adjustments to neuronal activity should be generated via energy minimisation before synaptic adjustment [19]. Synaptic weights may be modified to realise the preconceived activities in response to the given input stimuli [19], thereby transitioning from input information to label information through model layers. “Local neural synchronisation” generates target neural activity for hidden layers by projecting neuronal activity onto periodic basis vectors representative of class labels [24].

Going beyond these approaches, we propose the use of random nonlinear projections of both pre-synaptic inputs and target labels to generate local target activities in the forward pass. The objective of this approach is to develop a neural network training algorithm which requires no retrograde communication. Closed-form regression techniques are applicable in this setting, permitting single-step layer weight computation without error feedback. Thus, weight parameters are determined without backward communication from neuronal outputs or downstream layers. Further advantages of this method include the direct interpretability of hidden neurons with respect to local label predictions and stability in the few-shot setting.

## Results

We consider a dataset  $\mathcal{D} = \{(\mathbf{x}_i, \mathbf{y}_i)\}_{i=1}^N$  from the joint distribution  $(X, Y)$ . The task is to learn a feed-forward neural network function mapping  $X \rightarrow Y$ . The model has  $L$  layers, with dimensions  $m_0, \dots, m_L$ , and activations  $\mathbf{a}_0, \dots, \mathbf{a}_L$ , where  $\mathbf{a}_0 = \mathbf{x}$  and  $\mathbf{a}_L = \mathbf{y}$ . Each layer is equipped with weights  $\mathbf{W}_l$  to generate membrane potential  $\mathbf{z}_l = \mathbf{a}_{l-1} \mathbf{W}_l$ , and activation function  $f_l : \mathbb{R} \rightarrow \mathbb{R}$  to generate neuronal outputs  $\mathbf{a}_l = f_l(\mathbf{z}_l)$ . The model prediction is defined as  $\hat{\mathbf{y}} = f_L(\mathbf{W}_L(\dots f_1(\mathbf{W}_1 \mathbf{x})))$ .

### Forward Projection (FP)

To generate target membrane potentials for hidden neurons, we present the Forward Projection (FP) algorithm (Figure 1-A). We propose to combine pre-synaptic inputs and labels using random non-linear projections to generate targets (Figure 1-B). For each training sample, the target potential  $\tilde{\mathbf{z}}_l \in \mathbb{R}^{1 \times m_l}$  is generated from pre-synaptic inputs  $\mathbf{a}_{l-1} \in \mathbb{R}^{1 \times m_{l-1}}$  and labels  $\mathbf{y} \in \mathbb{R}^{1 \times m_L}$  using fixed random projection matrices  $\mathbf{Q}_l \in \mathbb{R}^{m_{l-1} \times m_l}$  and  $\mathbf{U}_l \in \mathbb{R}^{m_L \times m_l}$  such that

$$\tilde{\mathbf{z}}_l = g_l(\mathbf{a}_{l-1} \mathbf{Q}_l) + g_l(\mathbf{y} \mathbf{U}_l), \quad (1)$$

where  $g_l : \mathbb{R} \rightarrow \mathbb{R}$  is an element-wise non-linear transformation. It is noted here that  $g_l$  is not necessarily equal to  $f_l$ , the neural activation function.  $\mathbf{Q}_l$  and  $\mathbf{U}_l$  are fixed linear projections drawn from random Gaussian distributions, which are pre-defined before training. The target potential  $\tilde{\mathbf{z}}_l$  allows for a local auxiliary loss function to be defined with respect to the actual membrane potential,  $\mathbf{z}_l$ , realised during the forward pass. The randomised combination of pre-synaptic inputs with the target label is inspired by the high-dimensional computing paradigm [25], where fixed random projections are employed to encode information from multiple vector inputs, approximately preserving relative distances according to the Johnson-Lindenstrauss lemma [25]. Accordingly, it is noted that  $\tilde{\mathbf{z}}_l$  approximately encodes both  $\mathbf{a}_{l-1}$  and  $\mathbf{y}$  (see remark A.7 in SI). By generating target potentials in a forward manner, the mix of information encoded in each layer is expected to transition incrementally from predominantly input information in early layers to label information in later layers. We propose to define a local loss function  $\mathcal{L}_l := \|\mathbf{Z}_l - \tilde{\mathbf{Z}}_l\|$ , which may be employed as an objective to optimise  $\mathbf{W}_l$ . Synaptic weights for each layer can be computed in a closed-form forward manner, using ridge regression (Figure 1-C), such that

$$\mathbf{W}_l := (\mathbf{A}_{l-1}^T \mathbf{A}_{l-1} + \lambda \mathbf{I})^{-1} (\mathbf{A}_{l-1}^T \tilde{\mathbf{Z}}_l). \quad (2)$$

Here,  $\mathbf{A}_{l-1} \in \mathbb{R}^{N \times m_{l-1}}$  and  $\tilde{\mathbf{Z}}_l \in \mathbb{R}^{N \times m_l}$  are matrices of pre-synaptic activities and target potentials, respectively, collected over the  $N$  samples in  $\mathcal{D}$ .  $\lambda$  is a regularisation term and  $\mathbf{I}$  is the identity matrix. Observe that  $\mathbf{A}_{l-1}^T \mathbf{A}_{l-1}$  and  $\mathbf{A}_{l-1}^T \tilde{\mathbf{Z}}_l$  terms in (2) may be computed sequentially over instances  $\{\mathbf{a}_{1,l-1}, \dots, \mathbf{a}_{N,l-1}\} \subset \mathbb{R}^{1 \times m_{l-1}}$ , and  $\{\tilde{\mathbf{z}}_{1,l-1}, \dots, \tilde{\mathbf{z}}_{N,l-1}\} \subset \mathbb{R}^{1 \times m_l}$  (see remark A.6 in SI). Therefore, memory requirements are independent of  $N$ , depending only on  $m_{l-1}$  and  $m_l$ . The approach of encoding

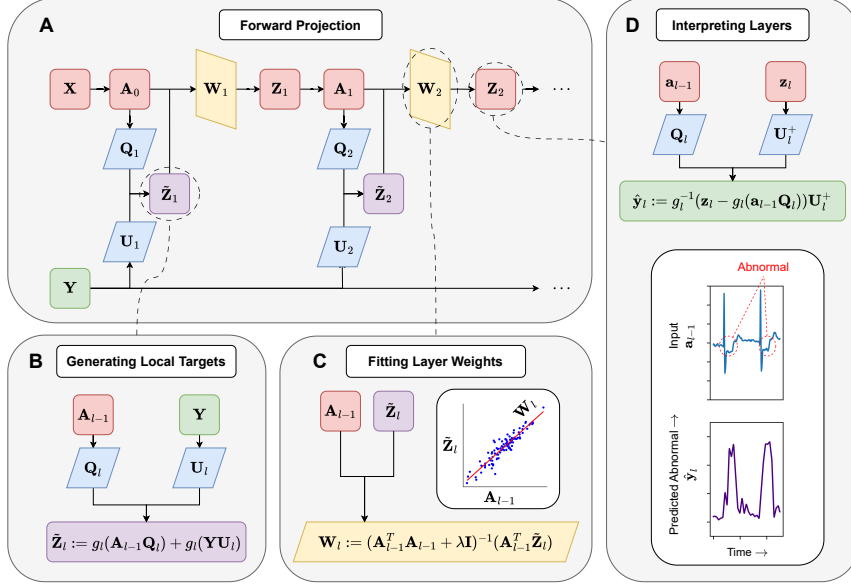


**Fig. 1:** A: Forward projection algorithm for fitting layer weights  $\mathbf{W}_1, \dots, \mathbf{W}_l$  to model labels  $\mathbf{Y}$  from data  $\mathbf{X}$ . B: Procedure for generating the  $l$ -th layer target potentials  $\tilde{\mathbf{z}}_l$ . Pre-synaptic inputs  $\mathbf{A}_{l-1}$  and labels  $\mathbf{Y}$  are projected with fixed matrices  $\mathbf{Q}_l$  and  $\mathbf{U}_l$ , respectively before applying non-linearity  $g_l$ . C: Optimising  $\mathbf{W}_l$  to predict  $\tilde{\mathbf{z}}_l$  from  $\mathbf{A}_{l-1}$  by ridge regression with penalty  $\lambda$ . D: Interpreting membrane potentials  $\mathbf{z}_l$  as a local label prediction  $\hat{\mathbf{y}}_l$  given pre-synaptic inputs  $\mathbf{a}_{l-1}$  and projection matrices  $\mathbf{Q}_l$  and  $\mathbf{U}_l^+$ , where  $\mathbf{U}_l^+$  is the pseudo-inverse of  $\mathbf{U}_l$ .

information on both inputs and labels in the hidden layers is inspired by the Predictive Coding and target propagation paradigms [1, 5, 9]. However, unlike previous approaches, no backward communication is required from neuronal outputs to pre-synaptic inputs to achieve the FP fit. As a consequence of this fitting approach, neural membrane potentials in hidden layers of FP-trained models may be interpreted as label predictions (Figure 1-C).

## Forward Projection Performance

Forward Projection was compared to other local learning methods, including random features (RF) [23], Local Supervision (LS) [9], and Forward-Forward (FF) [15] in multiple tasks using equivalent model architectures (Table 1). The Fashion MNIST (FMNIST) image classification task was modelled on a multi-layer perceptron (MLP). Forward projection achieved higher test accuracy than other local learning methods in this task, approaching the performance of the backpropagation reference standard. Two large-scale biomedical sequence modelling tasks were also evaluated with one-dimensional convolutional neural network (1d-CNN) architectures. The Promoters task required the identification of human non-TATA promoters, a class of gene

Dataset	Method Metric	FP (ours)	RF	LS	FF	PC	DTP	BP (ref.)
FMNIST MLP	AUC	98.3 ± 0.0	98.0 ± 0.0	98.7 ± 0.1	98.5 ± 0.1	98.2 ± 0.1	97.8 ± 0.2	99.0 ± 0.0
	Acc	86.3 ± 0.1	84.0 ± 0.2	83.1 ± 2.0	85.6 ± 0.8	83.0 ± 0.4	79.3 ± 2.0	88.4 ± 0.3
Promoters 1d-CNN	AUC	88.7 ± 0.5	80.0 ± 1.1	86.6 ± 1.1	83.5 ± 0.7	79.7 ± 1.7	78.8 ± 0.8	94.1 ± 0.3
	Acc	81.8 ± 0.5	72.2 ± 1.4	79.7 ± 1.2	75.3 ± 3.6	70.5 ± 3.6	69.3 ± 3.3	87.4 ± 0.7
PTBXL-MI 1d-CNN	AUC	95.5 ± 0.5	94.7 ± 1.8	97.3 ± 0.3	89.3 ± 3.8	86.0 ± 0.9	86.4 ± 2.2	99.3 ± 0.0
	Acc	86.5 ± 1.1	83.4 ± 2.1	86.1 ± 4.0	69.4 ± 8.2	64.2 ± 5.0	70.1 ± 5.8	94.9 ± 0.6
CIFAR 2d-ViT	AUC	91.5 ± 0.5	83.1 ± 0.5					96.1 ± 0.4
	Acc	83.5 ± 0.5	75.9 ± 0.6					89.2 ± 0.7

**Table 1:** Test performance of various learning methods across different datasets. The FMNIST dataset was modelled with a multi-layer perception; Promoters and PTBXL-MI datasets were modelled using 1D convolutional neural networks (1D-CNNs); and CIFAR was modelled using vision transformers. BP: backpropagation; DTP: Difference Target Propagation; FF: Forward Forward; FP: Forward Projection; LS: Local Supervision; PC: Predictive Coding; RF: random features

promoter regions which increase transcription of DNA sequences [26, 27]. Forward projection yielded higher test performance than all other local learning methods in this task. The PTBXL-MI task [28] required diagnosis of myocardial infarction (MI), a heart condition commonly known as “heart attack”, from 12-channel electrocardiograph (ECG) recordings. FP and LS performed comparably in this task. FP also outperformed all other methods in the optimisation of models with more complex neuronal activations such as modulo and polynomial activation functions (see remark A.11 in SI). FP was implemented in a transformer architecture to discriminate the first two classes of the CIFAR10 dataset, significantly outperforming random features.

Backpropagation performance benchmarks in PTBXL-MI and Promoters tasks were comparable to previous studies [27, 29].

### Alternative Feedback-free Approaches

To assess the value of the FP target generation function, we compared the performance of closed-form regression models fitted to targets generated by alternative functions, including simple label projection ( $\tilde{\mathbf{Z}}_l := \mathbf{y}\mathbf{U}_l$ ) and label projection with additive noise ( $\tilde{\mathbf{Z}}_l := \mathbf{y}\mathbf{U}_l + \mathbf{E}$ ). To evaluate the capability of feedback-free training methods to handle information “bottlenecks”, they were applied to optimise MLP architectures for FMNIST classification. MLPs were generated with 1000 hidden neurons in the first and second layers ( $m_1 = m_2 = 1000$ ), and  $m_3 \in \{100, 200, 400, 800\}$  neurons in the final hidden layer. FP outperformed other feedback-free approaches (Figure 2-A). The performance of RF deteriorated in models with small penultimate layers, as relevant information was less likely to be represented by random projection [23]. The performance of simple label projection deteriorated in models with large penultimate layers, a result which may be attributable to rank deficiency (see remark A.5 in SI). Noisy label projection maintained steady performance but at a lower level than FP.

### Few-Shot Learning

“Few-shot” learning is a constrained learning scenario in which the number of data samples available for training is small. High-dimensional data, such as images, pose a

challenge for few-shot learning, as many spurious features may exist. Thus, successful few-shot training methods must select generalisable features in the presence of these confounders. Few-shot learning was assessed in image classification tasks using a 2D-CNN architecture. The optical coherence tomography task (OCT) [30] required that the model discriminate images of healthy retinas from those with choroid neovascularization, a pathology that affects the eye and manifests mainly as abnormal growth of blood vessels behind the retina. The paediatric chest X-ray (CXR) task [30] required the model to discriminate between images of viral pneumonia, bacterial pneumonia, or healthy controls. The CIFAR task required the model to discriminate between the first two CIFAR10 classes (aeroplane and automobile). Few-shot training datasets were generated by subsampling, with  $N \in \{5, 10, 15, 20, 30, 40, 50\}$  training examples from each class for OCT and CXR tasks, and  $N \in \{25, 50, 75, 100\}$  training examples per class for the CIFAR task. Data augmentation was not employed. Model generalisability was assessed on all test data (CXR:  $N_{\text{test}} = 431$ ; OCT:  $N_{\text{test}} = 327$ , CIFAR:  $N_{\text{test}} = 2000$ ). Forward Projection-trained models demonstrated the greatest few-shot generalisability in CXR (Figure 2-B), OCT (Figure 2-C), outperforming all other methods, including backpropagation, in all the tasks with  $N \leq 40$  training samples. In the CIFAR few-shot task, Forward Projection achieved the best performance of any local learning method in experiments with  $N \in \{50, 75, 100\}$ , being outperformed only by backpropagation. With as few as  $N = 10$  training samples, Forward Projection fitted discriminative models for the classification of OCT (test AUC:  $84.5 \pm 5.8$ ) and CXR (test AUC:  $76.6 \pm 5.8$ ). CXR and OCT datasets highlighted two distinct vulnerabilities of backpropagation training in few-shot conditions. In the  $N = 5$  setting on OCT, backpropagation overfitted the training samples (Train AUC:  $86.8 \pm 13.2$ ; Test AUC:  $61.8 \pm 17.4$ ), as models integrated noise into decision functions. On the other hand, backpropagation failed to achieve adequate model fitting in the  $N = 10$  setting on CXR (Train AUC:  $69.0 \pm 8.1$ ; Test AUC:  $59.7 \pm 6.2$ ). Random features performed comparably to backpropagation in tasks with fewest training samples, but performance improved only slightly with larger sample sizes. Random Features models could not overfit within convolutional layers, as these contained no free parameters. However, Random Features had limited capacity to learn structural features in larger training samples. The improvement that Forward Projection provided over Random Features is therefore attributable to structural feature learning within hidden convolutional layers. Label Projection and Noisy Label Projection failed to converge in few-shot training (training AUC  $\approx 0.50$ ). Neither Local Supervision nor Forward-Forward training matched the baseline generalisability of Random Features in OCT and CXR tasks - however Local Supervision achieved comparable test discrimination to Forward Projection in the CIFAR task when  $N \geq 75$ . Predictive coding and Difference Target Propagation were yielded uninformative models in few-shot learning tasks (Figure A3). Few-shot performance is tabulated in Supplemental Table A2.

## Feature Interpretability

Explainability is a central issue with backpropagation-based learning, as relationships between hidden activations and model predictions may be non-monotonic, complicating the interpretation of hidden neural activities [31]. An important advantage of Forward Projection is the interpretability of hidden neuron activity with respect to label predictions (see remark A.7 in SI). Assuming  $\mathbf{z}_l \approx \tilde{\mathbf{z}}_l$ , neural potentials may be interpreted as a local label prediction  $\hat{\mathbf{y}}_l$  (Figure 1-D), such that

$$\hat{\mathbf{y}}_l := g_l^{-1}(\tilde{\mathbf{z}}_l - g_l(\mathbf{a}_{l-1}\mathbf{Q}_l))\mathbf{U}_l^+. \quad (3)$$

Here,  $\mathbf{U}_l^+$  is the Moore-Penrose generalised inverse of the label projection matrix. Likewise, pre-synaptic inputs are encoded in neural pre-activation potentials, with an analogous reconstruction function (see remark A.7 in SI). It is noted that (3) may be uninformative if  $\frac{\|\mathbf{z}_l - \tilde{\mathbf{z}}_l\|}{\|\tilde{\mathbf{z}}_l\|}$  is large – i.e. if  $\mathbf{W}_l$  did not achieve a good fit. Measurement of local error in training data may provide insights into the reliability of (3) during inference. Interpretation of pre-activation potentials  $z_l$  is simplified by selection of bijective functions for  $g_l$  so that  $g_l^{-1}$  exists everywhere. In practice, a surrogate approximation to the functional inverse was observed to suffice in our experiments; for example,  $g_l^{-1}(\cdot) \approx \tanh(\cdot)$  was employed as a surrogate inverse for  $g_l(\cdot) = \text{sign}(\cdot)$ . In our experiments, hidden neurons of models fitted with Forward Projection were interpretable as label predictions. In the FMNIST task, test accuracy of layer explanations was observed to improve between early layers and subsequent layers (Figure A2-A), demonstrating synergistic learning. In the PTBXL-MI task, applying the surrogate layer explanation function (described in equation(3)) to the convolutional layers identified various clinically salient features for diagnosing myocardial infarction (MI). MI, a clinical condition characterised by damage to heart muscles due to poor blood flow, may manifest in ECG data with various electro-physical abnormalities. Consequently, the model must learn several distinct pathological waveform features, including elevation of the so-called “ST” segment, or inversion of the “T”-wave. Figure 3-A shows the layer explanation functions as a function of time in four patients, three of whom were diagnosed with myocardial infarction. Patient A demonstrates ST-segment depression in lead II, which is temporally consistent with peaks in the model explanation functions at each layer. Likewise, the model explanation functions peak during ST-segment elevation in patient B and during QRS widening and T-wave inversion in Patient C. In contrast, the model explanation function is near zero in Patient D, who had normal ECG morphology. Forward Projection model explanations derived using (3) from the sixth convolutional layer ( $\hat{\mathbf{y}}_6$ ) were compared with GradCAM outputs of backpropagation-trained networks. The first 15 MI-positive test instances in the PTBXL dataset were annotated by a medical doctor to segment the diagnostically relevant subsequences. Layer explanations derived by Forward Projection achieved similar discrimination performance (AUC:  $0.61 \pm 0.14$ , AUPR:  $0.52 \pm 0.19$ ) to GradCAM (AUC:  $0.59 \pm 0.12$ , AUPR:  $0.55 \pm 1.3$ ) (Figure 3-B).

Choroid neovascularization (CNV) is the growth of abnormal blood vessels behind the retina due to diseases such as age-related macular degeneration [32]. In OCT images,

CNV may be represented by various image features, including hyper-reflective dots and detachment of the retinal pigment epithelium [33]. In the OCT task, the model’s explanation functions identified regions of interest related to CNV (Figure 4). 2D-CNN models trained with only 100 instances per class learned to localise fine-grained CNV features including retinal/subretinal fluid (Patients A-C), hard exudates (Patient B), and fibrosis (Patient C).

## Training Complexity

We now analyse the complexity of training with the Forward Projection algorithm for a classification task by estimating the storage and computational requirements for a densely connected  $m \times m$  hidden layer. We consider a dataset comprising of  $N$  training samples, with label dimension  $m_L$ . Note that FP model weights can be obtained in one pass over the  $N$  training samples, while all other methods require each training sample to be fed to the network for several epochs (denoted  $N_e$ ). The training procedure for each layer is presented in Supplementary Figure A1.

The memory requirement for Forward Projection is  $\mathcal{O}(m^2)$  for the layer weights,  $\mathcal{O}(m^2)$  for the  $Q$  matrix, and  $\mathcal{O}(mm_L)$  for the  $U$  matrix. As the  $\mathbf{A}_{l-1}^T \mathbf{A}_{l-1}$  and  $\mathbf{A}_{l-1}^T \tilde{\mathbf{Z}}_l$  terms in (2) can be accumulated sequentially over data batches (See Remark A.6 in SI), two  $m \times m$  matrices suffice for their storage, thereby avoiding storage of the  $N \times m$  matrices  $\mathbf{A}_{l-1}$  and  $\tilde{\mathbf{Z}}_l$ . As with all methods, Forward Projection requires  $\mathcal{O}(m^2)$  multiply-and-accumulate (MAC) operations to calculate the activations for the downstream layer in the forward pass. To generate target potentials during the forward pass, Forward Projection also requires  $\mathcal{O}(m^2)$  additional MAC operations to project through  $Q$  and  $\mathcal{O}(mm_L)$  MAC operations to project through  $U$ . Computation of the  $\mathbf{A}_{l-1}^T \mathbf{A}_{l-1}$  and  $\mathbf{A}_{l-1}^T \tilde{\mathbf{Z}}_l$  terms require  $\mathcal{O}(Nm^2)$  MAC operations each. After all samples have been observed, computation of model weights using equation (2) requires  $\mathcal{O}(m^3)$  operations to invert the  $\mathbf{A}_{l-1}^T \mathbf{A}_{l-1}$  term and  $\mathcal{O}(m^3)$  operations for matrix multiplication to complete the regression; however, this happens only once for each layer. Furthermore, Forward Projection requires no backward pass.

For backpropagation,  $\mathcal{O}(m^2)$  memory is required for storing layer weights,  $\mathcal{O}(m^2)$  for accumulated gradients, and  $\mathcal{O}(m)$  for activations. Here, the computation requirements scale as  $\mathcal{O}(N_e m^2)$  MACs each for the forward pass, backward pass, and weight update calculations. Hence, in the typical setting where  $m \gg m_L$ , we note that Forward Projection and backpropagation have similar memory requirements, scaling as  $\mathcal{O}(m^2)$ . Notably, compute scales as  $\mathcal{O}(m^3)$  for FP versus  $\mathcal{O}(N_e m^2)$  for BP. For example, training a dense hidden layer with 1000 inputs and 1000 outputs on the FMNIST dataset ( $N = 60,000$ ,  $m_L = 10$ ) by Forward Projection requires a total of  $1.2 \times 10^{11}$  MAC operations for the forward pass and  $1.2 \times 10^{11}$  operations for the weight update. Training the same layer via 100 epochs of backpropagation requires  $6.0 \times 10^{12}$  MAC operations for forward passes and  $1.2 \times 10^{13}$  operations for weight updates. Forward projection requires only a single training epoch, leading to a proportional speed up in the overall computation time. Note that Local Supervision and Forward-Forward algorithms have similar computational and memory requirements as backpropagation, as illustrated in Table 2. We also present the wall-clock time for full training of an

Method	Compute			Memory		FMNIST Training	
	Training epochs	Forward pass	Weight update	Model parameters	Weight update	Time (s)	Epochs
Backpropagation	$N_e$	$N_e N m^2$	$2N_e N m^2$	$m^2$	$m^2 + 2m$	$22.43 \pm 4.8$	$11.6 \pm 2.7$
Local Supervision	$N_e$	$N_e N (m^2 + m m_L)$	$N_e N (m^2 + m m_L)$	$m^2 + m m_L$	$m^2 + 2m$	$46.9 \pm 12.5$	$10.8 \pm 3.56$
Forward-Forward	$N_e$	$2N_e N m^2$	$N_e N m^2$	$m^2$	$m^2$	$172 \pm 56$	$40.2 \pm 13.8$
Predictive Coding	$N_e$	$N_e N m^2$	$4N_e N m^2$	$2m^2$	$2m^2 + 2m$	$150 \pm 61$	$25.4 \pm 10.2$
Difference Target Prop.	$N_e$	$N_e N m^2$	$8N_e N m^2$	$2m^2$	$2m^2 + 4m$	$72.7 \pm 26.4$	$13.6 \pm 5.3$
Forward Proj. (Ours)	1	$N(2m^2 + m m_L)$	$2N m^2 + 2m^3$	$2m^2 + m m_L$	$2m^2$	$0.34 \pm 0.1$	1

**Table 2:** Complexities of each training method in an MLP with  $m$  inputs, one output and  $L$  hidden layers of dimension  $m$ .  $N$ : training sample size.  $N_e$ : epochs, all parameters except activations are per layer.

MLP with  $3 \times 1000$  hidden neurons on FMNIST, demonstrating a  $66\times$  speedup with Forward Projection in this example. Further timing results are provided in Table A3 in SI. Computations were run using the Google Colab service with an NVIDIA T4 graphics processing unit.

## Discussion

We present the Forward Projection algorithm, which enables learning in a single pass over the dataset using random projections and closed-form optimisation. Compared to state-of-the-art local learning methods that require observing post-synaptic neuronal outputs to optimise synaptic weights via error-based gradient descent, Forward Projection operates under a stricter constraint, fitting weights using just the pre-synaptic neuronal activity and labels.

The target generation function proposed here for Forward Projection promotes input and label encoding in neural membrane potentials (see section A.7 in SI). Joint encoding of labels with pre-synaptic activity alleviates the degenerate neural activity which results from local modelling of simple label projections, whilst avoiding the introduction of uninformative noise (see section A.5 in SI). In this analysis, a simple non-linearity was employed for target generation. The utility of more complex nonlinearities for target generation is a subject for further research.

Explainability of neural network models is an important limitation in decision-critical fields such as biomedicine, where errors such as confounded decisions may lead to significant consequences [34]. FP-trained layers may be interpreted without downstream information, providing insight into model reasoning in hidden layers. FP interpretation yielded informative outputs in three model architectures, identifying clinically salient features in ECG sequences and OCT images. An important advantage of FP training is

that saliency maps may be generated before downstream fitting, permitting on-the-fly inspection of intermediate layers for sufficiency or confounding. Thus, expert scrutiny of hidden layer performance may be conducted even before downstream architecture is finalised.

Few-shot learning is ubiquitous in biological systems, which exhibit rapid neuronal adaptation to changing environments [35]. In our experiments, Forward Projection demonstrated clear performance advantages over backpropagation and local learning approaches in few-shot learning tasks, presenting a plausible method for learning new tasks rapidly. In this setting, convolutional features learned by Forward Projection yielded more generalisable models than backpropagation, which overfitted in some experiments and underfitted in others, even underperforming random features in some cases. Forward Projection performed similarly to Local Supervision and Forward-Forward training in these tasks. Forward Projection also maintained reasonable performance on activation functions which were untrainable by SGD-based methods (see section A.11 in SI).

The closed-form Forward Projection fit is computable in a single pass over the data for each layer, presenting an opportunity to expedite training and reduce environmental footprint. The efficiency of FP training is attributable to a substantially different operational sequence to that employed in SGD-based approaches. Firstly, FP training collects a gram matrix of pre-synaptic activity over a single epoch, which is subsequently inverted during a one-step weight matrix computation. Secondly, FP completes fitting for each layer before initialising successive layers. In contrast, SGD-based approaches fit all the layers in the network iteratively, using feedback from neuronal outputs and downstream layers. FP training requires no retrograde communication between neural output activations and pre-synaptic connections, enabling direct training on hardware with unidirectional synaptic and neuronal communication. This differs from current iterative local learning methods, which require backward communication from neuronal outputs to optimise pre-synaptic parameters (see section A.1 in SI). Although FP addresses the feedback-free constraint of biological learning systems, the biological plausibility of one-step learning through matrix inversion is uncertain. Forward Projection training may be applicable as a pre-training step to reduce the number of training epochs required for backpropagation.

In conclusion, FP is an efficient approach for neural network optimisation, employing techniques from randomised projective embedding and linear regression to fit weight matrices in one epoch using a single-step solution. Interpretability of hidden neurons in FP-trained models may be employed to improve the explainability of neural network predictions.

## Methods

Generalisability of machine learning methods to real-world datasets requires robustness to adverse modelling conditions such as class imbalance and noise, which often impede performance [36]. To assess the applicability and generalisability of Forward

Projection and local learning methods in diverse real-world conditions, performance was evaluated in benchmark tasks from four biomedical domains described below.

### **PTBXL-MI**

The PTB-XL dataset contains 12-lead electrocardiography (ECG) recordings from 18,889 participants [28, 37]. ECG recordings of ten-second duration and 100Hz sample rate were used in our experiments. The predictive task was to discriminate ECG recordings with normal waveform morphology ( $N_{\text{train}} = 6,451; N_{\text{test}} = 721$ ) from those diagnosed as myocardial infarction ( $N_{\text{train}} = 2,707; N_{\text{test}} = 268$ ) by a cardiologist. Data instances with uncertain diagnoses were excluded from this analysis. Following recommendations of the data providers who provided predefined participant-disjoint dataset splits, the tenth fold was held out for model testing [28]. The first 15 MI-positive ECGs in the test set were annotated by a medical doctor to identify diagnostically relevant sections for quantitative explainability evaluation.

### **Promoters**

The Human Non-TATA Promoters dataset (“Promoters”) was extracted from the GenomicBenchmarks repository [27]. Data was originally published in [26]. 36,131 nucleotide sequences of 251 bases each were analysed. Nucleotide sequences were converted to 4-channel one-hot vectors indicating adenine, cytosine, guanine and thymine. Indeterminate bases were represented with zero vectors. Models were required to classify the promoter functionality of the sequence as “promoter” ( $N_{\text{train}} = 12,355; N_{\text{test}} = 4,119$ ) or “non-promoter” ( $N_{\text{train}} = 14,742; N_{\text{test}} = 4,915$ ).

### **CXR**

The paediatric pneumonia chest X-ray dataset (“CXR”) is a retrospective cohort of patients aged between one and five years, recorded in Guangzhou Women and Children’s Medical Center, Guangzhou, originally published in [30]. Chest X-ray images were recorded as part of routine care during diagnostic workup for suspected lower respiratory tract infection. During data collection, clinicians screened the images for quality and excluded those with severe artefact or corruption. Images were annotated by two expert physicians. Local institutional review board approvals were obtained. Images were loaded in greyscale, rescaled to the  $[0, 1]$  intensity range and resized to  $128 \times 128$  pixels by bilinear interpolation. Models were required to classify images “normal” ( $N_{\text{train}} = 1,349; N_{\text{test}} = 234$ ), “viral pneumonia” ( $N_{\text{train}} = 2,538; N_{\text{test}} = 242$ ), or “bacterial pneumonia” ( $N_{\text{train}} = 1,345; N_{\text{test}} = 148$ ).

### **OCT**

The optical coherence tomography dataset (“OCT”) is a retrospective cohort of adult patients from five ophthalmology institutions in the USA and China recorded between 2013 and 2017 during routine care, originally published in [30]. Images were initially annotated by local medical students, who had received OCT interpretation training. Subsequent annotation was performed by four ophthalmologists and two independent

retinal specialists. Horizontal foveal cut images were available in portable network graphics image format. Images were loaded in greyscale, rescaled to the  $[0, 1]$  intensity range, and resized to  $128 \times 128$  pixels by bilinear interpolation. Models were required to classify images as one of “normal” ( $N_{\text{train}} = 2,926; N_{\text{test}} = 149$ ) or “choroid neovascularisation” ( $N_{\text{train}} = 791; N_{\text{test}} = 178$ ).

## Model Training

The FMNIST dataset was modelled using an MLP with  $3 \times 1000$  hidden ReLU-activated neurons. Sequential datasets (PTBXL-MI and Promoters) were modelled by a 1d-CNN architecture of four convolutional blocks. Each convolutional block included two convolutional layers with kernel dimension 3, and strides of 1 and 2 respectively. Convolutional layers in the  $l$ -th block had  $32 \times 2^{l-1}$  filters. Convolutional implementation is detailed in Supplementary section A.2. Convolutional outputs were aggregated by global average pooling in the penultimate layer. For gradient-descent-based learning algorithms, batch normalisation layers were included between convolutional blocks. CIFAR modelling in Table 1 used a vision transformer architecture [38] operating on image patches of dimension  $4 \times 4$ , with a sequential stack of four multi-headed attention layers, each having 8 heads, embedding dimension 64, and MLP dimension 64. Few-shot image modelling tasks used a 2d-CNN architecture with kernel dimension  $3 \times 3$  and either  $16 \times 2^{l-1}$  filters in the  $l$ -th convolutional block (CXR and OCT) or  $32 \times 2^{l-1}$  filters in the  $l$ -th convolutional block (CIFAR). The sign function was employed to generate target activations for Forward Projection models, such that

$$\tilde{\mathbf{z}}_l = \text{sign}(\mathbf{a}_{l-1} \mathbf{Q}_l) + \text{sign}(\mathbf{y} \mathbf{U}_l). \quad (4)$$

Data augmentation was not performed in our experiments. Models were fitted using the PyTorch library. For SGD-based methods, early stopping was performed according to validation loss. Model weight initialisation was random, and optimisation was performed with the Adam optimiser with a learning rate of 0.001, training to minimise validation loss by early stopping with a patience of five epochs. In few-shot experiments, the learning rate was reduced to 0.0001 for SGD-based models and a patience of ten epochs was employed. It is acknowledged that direct comparison of gradient descent based training with closed-form solutions is not strictly “like-for-like”. However, all efforts were made to ensure experimental conditions were otherwise equivalent. Models were fitted to minimise categorical or binary cross-entropy as appropriate. Implementations of Forward-Forward, Local Supervision, Difference Target Propagation and Predictive Coding methods are detailed in supplementary section A.4.

## Explainability Analysis

Model architectures for explainability analysis were equivalent to those used for the main experiments. Pre-activation potentials in hidden neurons were interpreted as local label predictions using the approximation to (3) as

$$\hat{\mathbf{y}}_l := \tanh(\mathbf{z}_l - \text{sign}(\mathbf{a}_{l-1} \mathbf{Q}_l)) \mathbf{U}_l^+. \quad (5)$$

Here,  $\tanh(\cdot)$  is employed as a surrogate inverse for the sign function used to generate the target potentials.

## Declarations

### Funding

This research was supported in part by the EPSRC Open Fellowship EP/X011356/1.

### Competing Interests

Robert O’Shea contributed to the initial draft of the manuscript whilst employed at King’s College London. He commenced employment with Eli Lilly & Company prior to the submission of the revised manuscript. His involvement in this project is entirely independent of his role at Eli Lilly & Company and was not influenced by his employment there.

### Ethics approval and consent to participate

This study involves no new data collection or experiments on human or animal subjects. All clinical data used in this study was publicly available in previous publications [26–28, 30].

### Data Availability

The PTBXL-MI dataset is available from PhysioNet [37]. The Promoters dataset is available from the GenomicBenchmarks library [27] and the original publication [26]. The CXR and OCT datasets are provided in [30]. Pre-processed datasets and cross-validation folds are available for download at [fp\\_datasets - Mendeley Data](#) [39].

### Code Availability

All code required to reproduce study findings is available from [github.com/robertoshea/forward\\_projection](https://github.com/robertoshea/forward_projection).

### Author Contribution

**Robert O’Shea:** conceptualisation, methodology, formal analysis, software, investigation, visualisation, writing – original draft preparation. **Bipin Rajendran:** conceptualisation, methodology, supervision, writing – review & editing, resources, project administration, funding acquisition.

## Abbreviations

1d-CNN: one-dimensional convolutional neural network

2d-CNN: two-dimensional convolutional neural network

BP: backpropagation

CNN: convolutional neural network

CNV: choroid neovascularisation  
CXR: chest x-ray (dataset)  
DTP: Difference Target Propagation  
ECG: electrocardiography  
FF: Forward-Forward algorithm  
FMNIST: FashionMNIST dataset  
FP: Forward Projection algorithm  
LP: label projection  
LPN: noisy label projection  
LS: Local Supervision  
MAC: multiply and accumulate  
MI: myocardial infarction  
MLP: multi-layer perceptron  
OCT: optical coherence tomography (dataset)  
PC: Predictive Coding  
PTBXL: PTBXL dataset  
RF: random features  
SGD: stochastic gradient descent

## References

- [1] Lee, D., Zhang, S., Fischer, A. & Bengio, Y. Appice, A. *et al.* (eds) *Difference target propagation*. (eds Appice, A. *et al.*) *Machine Learning and Knowledge Discovery in Databases - European Conference, ECML PKDD 2015, Porto, Portugal, September 7-11, 2015, Proceedings, Part I*, Vol. 9284 of *Lecture Notes in Computer Science*, 498–515 (Springer, 2015). URL [https://doi.org/10.1007/978-3-319-23528-8\\_31](https://doi.org/10.1007/978-3-319-23528-8_31).
- [2] Lillicrap, T. P., Cownden, D., Tweed, D. B. & Akerman, C. J. Random synaptic feedback weights support error backpropagation for deep learning. *Nature Communications* **7** (2016). URL <http://dx.doi.org/10.1038/ncomms13276>.
- [3] Lillicrap, T. P., Santoro, A., Marris, L., Akerman, C. J. & Hinton, G. Backpropagation and the brain. *Nature Reviews Neuroscience* **21**, 335–346 (2020). URL <http://dx.doi.org/10.1038/s41583-020-0277-3>.
- [4] Crick, F. The recent excitement about neural networks. *Nature* **337**, 129–132 (1989). URL <http://dx.doi.org/10.1038/337129a0>.
- [5] Millidge, B., Seth, A. K. & Buckley, C. L. Predictive coding: a theoretical and experimental review. *CoRR* **abs/2107.12979** (2021). URL <https://arxiv.org/abs/2107.12979>.
- [6] Burbank, K. S. & Kreiman, G. Depression-biased reverse plasticity rule is required for stable learning at top-down connections. *PLoS Computational Biology* **8**, e1002393 (2012). URL <http://dx.doi.org/10.1371/journal.pcbi.1002393>.

- [7] Akrouf, M., Wilson, C., Humphreys, P. C., Lillicrap, T. P. & Tweed, D. B. Wallach, H. M. *et al.* (eds) *Deep learning without weight transport.* (eds Wallach, H. M. *et al.*) *Advances in Neural Information Processing Systems 32: Annual Conference on Neural Information Processing Systems 2019, NeurIPS 2019, December 8-14, 2019, Vancouver, BC, Canada*, 974–982 (2019). URL <https://proceedings.neurips.cc/paper/2019/hash/f387624df552cea2f369918c5e1e12bc-Abstract.html>.
- [8] Friston, K. Hierarchical models in the brain. *PLoS Computational Biology* **4**, e1000211 (2008). URL <http://dx.doi.org/10.1371/journal.pcbi.1000211>.
- [9] Bengio, Y., Lamblin, P., Popovici, D. & Larochelle, H. Schölkopf, B., Platt, J. C. & Hofmann, T. (eds) *Greedy layer-wise training of deep networks.* (eds Schölkopf, B., Platt, J. C. & Hofmann, T.) *Advances in Neural Information Processing Systems 19, Proceedings of the Twentieth Annual Conference on Neural Information Processing Systems, Vancouver, British Columbia, Canada, December 4-7, 2006*, 153–160 (MIT Press, 2006). URL <https://proceedings.neurips.cc/paper/2006/hash/5da713a690c067105aeb2fae32403405-Abstract.html>.
- [10] Kaiser, J., Mostafa, H. & Neftci, E. Synaptic plasticity dynamics for deep continuous local learning (decolle). *Frontiers in Neuroscience* **14** (2020). URL <http://dx.doi.org/10.3389/fnins.2020.00424>.
- [11] Frenkel, C., Lefebvre, M. & Bol, D. Learning without feedback: Fixed random learning signals allow for feedforward training of deep neural networks. *Frontiers in Neuroscience* **15** (2021). URL <http://dx.doi.org/10.3389/fnins.2021.629892>.
- [12] Wang, Y., Ni, Z., Song, S., Yang, L. & Huang, G. Mohamed, S. (ed.) *Revisiting locally supervised learning: an alternative to end-to-end training.* (ed. Mohamed, S.) *9th International Conference on Learning Representations, ICLR 2021, Virtual Event, Austria, May 3-7, 2021* (Openreview.net, 2021). URL <https://iclr.cc/virtual/2021/poster/3135>.
- [13] Tang, M., Yang, Y. & Amit, Y. Biologically plausible training mechanisms for self-supervised learning in deep networks. *Frontiers Comput. Neurosci.* **16** (2022). URL <https://doi.org/10.3389/fncom.2022.789253>.
- [14] Amit, Y. Deep learning with asymmetric connections and hebbian updates. *Frontiers Comput. Neurosci.* **13**, 18 (2019). URL <https://doi.org/10.3389/fncom.2019.00018>.
- [15] Hinton, G. E. The forward-forward algorithm: Some preliminary investigations. *CoRR* **abs/2212.13345** (2022). URL <https://doi.org/10.48550/arXiv.2212.13345>.
- [16] Dellaferrera, G. & Kreiman, G. Chaudhuri, K. *et al.* (eds) *Error-driven input modulation: Solving the credit assignment problem without a backward pass.*

- (eds Chaudhuri, K. *et al.*) *Proceedings of the 39th International Conference on Machine Learning*, Vol. 162 of *Proceedings of Machine Learning Research*, 4937–4955 (PMLR, 2022). URL <https://proceedings.mlr.press/v162/dellaferreira22a.html>.
- [17] Srinivasan, R. F. *et al.* Kim, B. (ed.) *Forward learning with top-down feedback: Empirical and analytical characterization*. (ed. Kim, B.) *The Twelfth International Conference on Learning Representations, ICLR 2024, Vienna, Austria, May 7-11, 2024* (OpenReview.net, 2024). URL <https://iclr.cc/virtual/2024/poster/18804>.
- [18] Pau, D. P. & Aymone, F. M. Demrozi, F. (ed.) *Suitability of forward-forward and PEPITA learning to mlcommons-tiny benchmarks*. (ed. Demrozi, F.) *IEEE International Conference on Omni-layer Intelligent Systems, COINS 2023, Berlin, Germany, July 23-25, 2023*, 1–6 (IEEE, 2023). URL <https://doi.org/10.1109/COINS57856.2023.10189239>.
- [19] Song, Y. *et al.* Inferring neural activity before plasticity as a foundation for learning beyond backpropagation. *Nature Neuroscience* **27**, 348–358 (2024). URL <http://dx.doi.org/10.1038/s41593-023-01514-1>.
- [20] Ororbia, A. G. & Mali, A. A. Stone, P. (ed.) *Biologically motivated algorithms for propagating local target representations*. (ed. Stone, P.) *The Thirty-Third AAAI Conference on Artificial Intelligence, AAAI 2019, Honolulu, Hawaii, USA, January 27 - February 1, 2019*, 4651–4658 (AAAI Press, 2019). URL <https://doi.org/10.1609/aaai.v33i01.33014651>.
- [21] Ororbia, A. G., Mali, A. A., Kifer, D. & Giles, C. L. Williams, B., Chen, Y. & Neville, J. (eds) *Backpropagation-free deep learning with recursive local representation alignment*. (eds Williams, B., Chen, Y. & Neville, J.) *Thirty-Seventh AAAI Conference on Artificial Intelligence, AAAI 2023, Washington, DC, USA, February 7-14, 2023*, 9327–9335 (AAAI Press, 2023). URL <https://doi.org/10.1609/aaai.v37i8.26118>.
- [22] Rahimi, A. & Recht, B. Platt, J. C. *et al.* (eds) *Random features for large-scale kernel machines*. (eds Platt, J. C. *et al.*) *Proc. Advances in Neural Information Processing Systems 20*, 1177–1184 (Curran, 2007). URL <https://proceedings.neurips.cc/paper/2007/hash/013a006f03dbc5392effeb8f18fda755-Abstract.html>.
- [23] Yehudai, G. & Shamir, O. Wallach, H. M. *et al.* (eds) *On the power and limitations of random features for understanding neural networks*. (eds Wallach, H. M. *et al.*) *Advances in Neural Information Processing Systems 32: Annual Conference on Neural Information Processing Systems 2019, NeurIPS 2019, December 8-14, 2019, Vancouver, BC, Canada*, 6594–6604 (2019). URL <https://proceedings.neurips.cc/paper/2019/hash/5481b2f34a74e427a2818014b8e103b0-Abstract.html>.

- [24] Apolinario, M. P. E., Roy, A. & Roy, K. LLS: local learning rule for deep neural networks inspired by neural activity synchronization. *CoRR* **abs/2405.15868** (2024). URL <https://doi.org/10.48550/arXiv.2405.15868>.
- [25] Kanerva, P. Hyperdimensional computing: An introduction to computing in distributed representation with high-dimensional random vectors. *Cogn. Comput.* **1**, 139–159 (2009). URL <https://doi.org/10.1007/s12559-009-9009-8>.
- [26] Umarov, R. K. & Solovyev, V. V. Recognition of prokaryotic and eukaryotic promoters using convolutional deep learning neural networks. *PLOS ONE* **12**, e0171410 (2017). URL <http://dx.doi.org/10.1371/journal.pone.0171410>.
- [27] Grešová, K., Martinek, V., Čechák, D., Šimeček, P. & Alexiou, P. Genomic benchmarks: a collection of datasets for genomic sequence classification. *BMC Genomic Data* **24** (2023). URL <http://dx.doi.org/10.1186/s12863-023-01123-8>.
- [28] Wagner, P. *et al.* PTB-XL, a large publicly available electrocardiography dataset. *Scientific Data* **7** (2020). URL <http://dx.doi.org/10.1038/s41597-020-0495-6>.
- [29] Anand, A., Kadian, T., Shetty, M. K. & Gupta, A. Explainable AI decision model for ECG data of cardiac disorders. *Biomedical Signal Processing and Control* **75**, 103584 (2022). URL <http://dx.doi.org/10.1016/j.bspc.2022.103584>.
- [30] Kermany, D. S. *et al.* Identifying medical diagnoses and treatable diseases by image-based deep learning. *Cell* **172**, 1122–1131.e9 (2018). URL <http://dx.doi.org/10.1016/j.cell.2018.02.010>.
- [31] Saeed, W. & Omlin, C. W. Explainable AI (XAI): A systematic meta-survey of current challenges and future opportunities. *Knowl. Based Syst.* **263**, 110273 (2023). URL <https://doi.org/10.1016/j.knosys.2023.110273>.
- [32] Wang, R., Liang, Z. & Liu, X. Diagnostic accuracy of optical coherence tomography angiography for choroidal neovascularization: a systematic review and meta-analysis. *BMC Ophthalmology* **19** (2019). URL <http://dx.doi.org/10.1186/s12886-019-1163-5>.
- [33] Metrangolo, C. *et al.* Oct biomarkers in neovascular age-related macular degeneration: A narrative review. *Journal of Ophthalmology* **2021**, 1–16 (2021). URL <http://dx.doi.org/10.1155/2021/9994098>.
- [34] Leming, M., Das, S. & Im, H. Construction of a confounder-free clinical mri dataset in the mass general brigham system for classification of alzheimer’s disease. *Artificial Intelligence in Medicine* **129**, 102309 (2022). URL <http://dx.doi.org/10.1016/j.artmed.2022.102309>.
- [35] Benda, J. Neural adaptation. *Current Biology* **31**, R110–R116 (2021). URL <http://dx.doi.org/10.1016/j.cub.2020.11.054>.

- [36] O’Shea, R., Katti, P. & Rajendran, B. Mitsis, G. (ed.) *Baseline drift tolerant signal encoding for ECG classification with deep learning*. (ed. Mitsis, G.) *46th Annual International Conference of the IEEE Engineering in Medicine and Biology Society, EMBC 2024, Orlando, FL, USA, July 15-19, 2024*, 1–5 (IEEE, 2024). URL <https://doi.org/10.1109/EMBC53108.2024.10782759>.
- [37] Goldberger, A. L. *et al.* Physiobank, physiobank, and physionet: Components of a new research resource for complex physiologic signals. *Circulation* **101** (2000). URL <http://dx.doi.org/10.1161/01.cir.101.23.e215>.
- [38] Dosovitskiy, A. *et al.* An image is worth 16x16 words: Transformers for image recognition at scale (2021). URL <https://openreview.net/forum?id=YicbFdNTTy>.
- [39] O’Shea, R. fp\_datasets (2025). URL <https://data.mendeley.com/datasets/fb7xddyxs4/2>.
- [40] Wang, J., Chen, L. & Ng, C. W. W. Candan, K. S., Liu, H., Akoglu, L., Dong, X. L. & Tang, J. (eds) *A new class of polynomial activation functions of deep learning for precipitation forecasting*. (eds Candan, K. S., Liu, H., Akoglu, L., Dong, X. L. & Tang, J.) *WSDM ’22: The Fifteenth ACM International Conference on Web Search and Data Mining, Virtual Event / Tempe, AZ, USA, February 21 - 25, 2022*, 1025–1035 (ACM, 2022). URL <https://doi.org/10.1145/3488560.3498448>.
- [41] Glorot, X. & Bengio, Y. Teh, Y. W. & Titterton, D. M. (eds) *Understanding the difficulty of training deep feedforward neural networks*. (eds Teh, Y. W. & Titterton, D. M.) *Proceedings of the Thirteenth International Conference on Artificial Intelligence and Statistics, AISTATS 2010, Chia Laguna Resort, Sardinia, Italy, May 13-15, 2010*, Vol. 9 of *JMLR Proceedings*, 249–256 (JMLR.org, 2010). URL <http://proceedings.mlr.press/v9/glorot10a.html>.

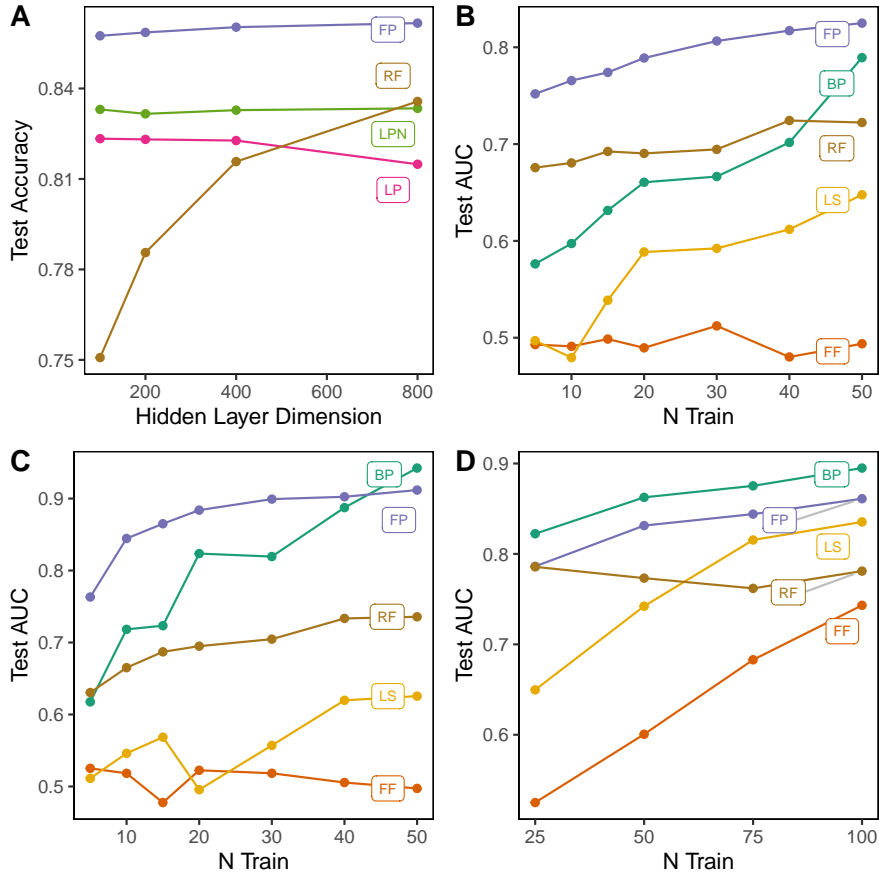


**Fig. 2:** A: Comparison of feedback-free fitting methods on FMNIST. MLP architectures had 1000 neurons in the first and second layers and 100, 200, 400 or 800 neurons in the final hidden layer. B-D: Test performance of few-shot trained 2D-CNN models. Mean test AUC is reported over 50 few-shot training experiments. B: Chest X-ray (CXR) task. C: Optical Coherence Tomography (OCT) task. D: CIFAR task in which models were required to classify the first two classes (aeroplane and automobile). Mean test AUC is reported over 50 few-shot training experiments. Models were fitted with  $N \in \{5, 10, 15, 20, 30, 40, 50\}$  training samples from each class in CXR and OCT tasks and  $N \in \{25, 50, 75, 100\}$  samples per class for the CIFAR task. Predictive Coding and Difference Target Propagation are plotted separately in Supplementary Figure A3. BP: backpropagation; FF: Forward-Forward; FP: Forward Projection; LS: Local Supervision; RF: random features.

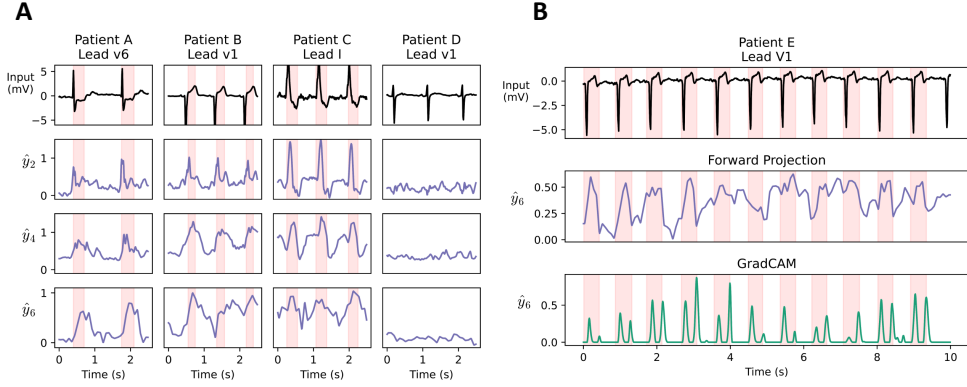


**Fig. 3:** A: Visualisation of layer explanations over time in a 1D-convolutional neural network trained by Forward Projection to detect myocardial infarction (MI) in electrocardiograms (ECGs) from PTBXL data. Patients A, B, C, E (diagnosed MI) and patient D (no disease) were extracted from test data. Explanations were extracted from the second, fourth and sixth convolutional layers ( $\hat{y}_2$ ,  $\hat{y}_4$ ,  $\hat{y}_6$ ) using equation (3). Explanations increase with MI features (highlighted in red), including ST-segment depression (Patient A), ST-segment elevation (Patient B) and QRS widening with T-wave inversion (Patient C). B: Comparison of Forward Projection with GradCAM. Above: ECG data from Patient E (diagnosed MI), showing ST-segment elevation. Middle: Sixth convolutional layer explanation ( $\hat{y}_6$ ) from a model trained by Forward Projection. Below: GradCAM output for the sixth convolutional layer of a model trained by backpropagation.

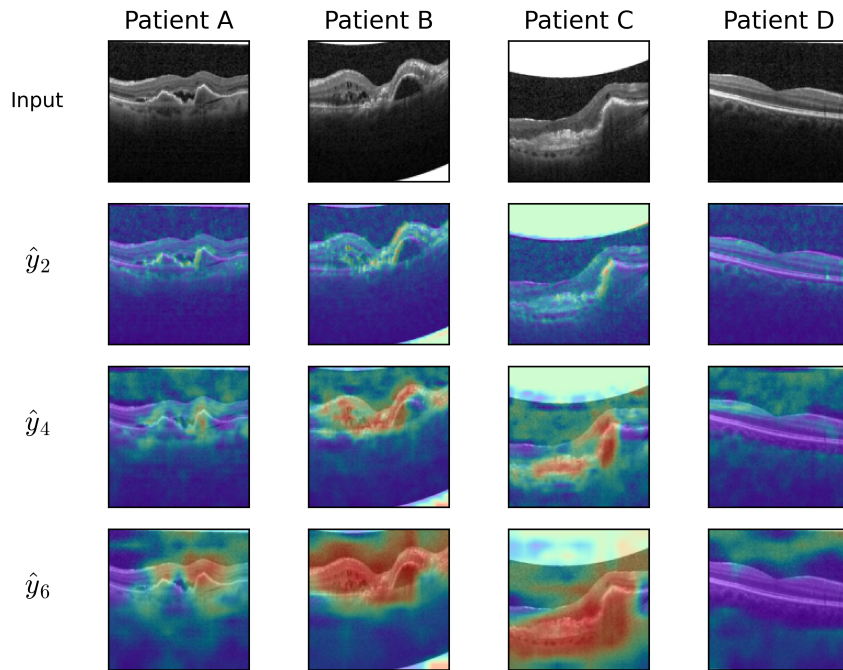


**Fig. 4:** Visualisation of layer explanations over space in 2D-convolutional neural networks trained by Forward Projection to detect choroid neovascularization (CNV) in the OCT task. Ensemble average of five models shown. Patients A-C, (diagnosed CNV) and patient D (no disease) were extracted from test data. Explanations were extracted from the second, fourth and sixth convolutional layers ( $\hat{y}_2, \hat{y}_4, \hat{y}_6$ ), using (3). CNV heat-maps demonstrate high values (red) over CNV features, including retinal/sub-retinal fluid (Patients A-C) and hard exudates (Patient B), and fibrosis (Patient C), with low values (blue) over healthy retina (Patient D).

## Appendix A Supplementary Information

### A.1 Local Learning Methods

Figure A1 illustrates training procedures and information flows in forward-projection, local-supervision, Forward-Forward and backpropagation algorithms.

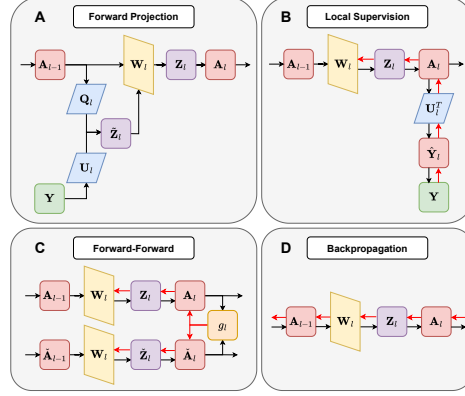


**Fig. A1:** Training Procedures for Forward Projection, Local Supervision, Forward Forward and Backpropagation learning algorithms for the  $l$ -th hidden layer. A: Forward Projection generates target matrix  $\tilde{\mathbf{Z}}_l$  by projecting pre-synaptic inputs  $\mathbf{A}_{l-1}$  by  $\mathbf{Q}_l$  and labels  $\mathbf{Y}$  by  $\mathbf{U}_l$ . Weights  $\mathbf{W}_l$  are fitted by regression, generating membrane potential  $\mathbf{Z}_l = \mathbf{A}_{l-1} \mathbf{W}_l$ . B: In Local Supervision, an auxiliary prediction  $\hat{\mathbf{Y}}_l$  is generated as a projection of the post-synaptic outputs  $\mathbf{A}_l$ , and  $\mathbf{W}_l$  is updated by a short backward pass (red arrows). C: In Forward-Forward, “positive” and “negative” pre-synaptic activities,  $\mathbf{A}_l$  and  $\bar{\mathbf{A}}_l$ , are generated from true and spurious data-label pairs, respectively.  $\mathbf{W}_l$  is updated to maximise positive activity whilst minimising negative activity. D: In backpropagation,  $\mathbf{W}_l$  is updated along its gradient with respect to the backpropagated error.

### A.2 Convolutional Layer Implementation for FP

We consider implementation of Forward Projection in a 2D convolutional layer over pre-synaptic input  $\mathbf{a}_{l-1} \in \mathbb{R}^{1 \times m_{l-1} \times R \times C}$ , having  $m_{l-1}$  channels, and spatial dimensions  $R \times C$  representing rows and columns. The  $k_1 \times k_2$  convolutional kernel positioned in row  $r \in \{1, \dots, R\}$  and column  $c \in \{1, \dots, C\}$  is represented in “flattened” form as  $\mathbf{a}_{l-1,r,c} \in \mathbb{R}^{1 \times (m_{l-1} k_1 k_2)}$ . This pre-synaptic input is projected by the constant matrix  $\mathbf{Q}_l \in \mathbb{R}^{(m_{l-1} k_1 k_2) \times m_l}$  to generate local target potentials  $\tilde{\mathbf{z}}_{l,r,c} \in \mathbb{R}^{1 \times m_l}$ , such that

$$\tilde{\mathbf{z}}_{l,r,c} = g_l(\mathbf{a}_{l-1,r,c} \mathbf{Q}_l) + g_l(\mathbf{y} \mathbf{U}_l). \quad (\text{A1})$$

Weights were fitted such that

$$\mathbf{W}_l := \left( \sum_{r=1}^R \sum_{c=1}^C \mathbf{A}_{l-1,r,c}^T \mathbf{A}_{l-1,r,c} + \lambda \mathbf{I} \right)^{-1} \left( \sum_{r=1}^R \sum_{c=1}^C \mathbf{A}_{l-1,r,c}^T \tilde{\mathbf{Z}}_{l,r,c} \right). \quad (\text{A2})$$

Here,  $\mathbf{A}_{l-1,r,c} \in \mathbb{R}^{N \times (m_{l-1} k_1 k_2)}$  is a matrix representing the pre-synaptic input for the convolutional kernel in row  $r$  and column  $c$  of the  $l$ -th layer over all  $N$  training instances. Likewise,  $\tilde{\mathbf{Z}}_{l,r,c} \in \mathbb{R}^{N \times m_l}$  contains target potentials for the kernel in row  $r$  and column  $c$  of the  $l$ -th layer over all  $N$  training instances. In each task, the FP penalty parameter was fixed at  $\lambda = 10$  for hidden layers and  $\lambda = 1$  for output layers. To prevent numerical overflow due to large layers or training datasets, a scalar reduction factor  $\tau \in (0, 1]$  may be applied to downscale  $\mathbf{A}^T \mathbf{A}$ ,  $\lambda$ , and  $\mathbf{A}^T \mathbf{Z}$  as necessary, such that:

$$\mathbf{W}_l := \left( \sum_{r=1}^R \sum_{c=1}^C \tau \mathbf{A}_{l-1,r,c}^T \mathbf{A}_{l-1,r,c} + \tau \lambda \mathbf{I} \right)^{-1} \left( \sum_{r=1}^R \sum_{c=1}^C \tau \mathbf{A}_{l-1,r,c}^T \tilde{\mathbf{Z}}_{l,r,c} \right). \quad (\text{A3})$$

### A.3 Attention Layer Implementation for FP

We consider the implementation of Forward Projection in a transformer layer over pre-synaptic input  $\mathbf{a}_{l-1} \in \mathbb{R}^{1 \times R \times m_{l-1}}$ , with  $R$  patches, each having  $m_{l-1}$  channels. Each attention head of dimension  $d \in \mathbb{N}$  contains three weight matrices for optimisation:  $\mathbf{W}_l^{\text{Query}}$ ,  $\mathbf{W}_l^{\text{Key}}$  and  $\mathbf{W}_l^{\text{Value}}$ , yielding intermediate activations  $\mathbf{z}_l^{\text{Query}} = \mathbf{a}_{l-1} \mathbf{W}_l^{\text{Query}}$ ,  $\mathbf{z}_l^{\text{Key}} = \mathbf{a}_{l-1} \mathbf{W}_l^{\text{Key}}$ , and  $\mathbf{z}_l^{\text{Value}} = \mathbf{a}_{l-1} \mathbf{W}_l^{\text{Value}}$  respectively. The attention scores  $\mathbf{s}_l$  are then calculated as

$$\mathbf{s}_l := \text{Softmax} \left( \frac{\mathbf{z}_l^{\text{Query}} \times (\mathbf{z}_l^{\text{Key}})^T}{\sqrt{d}} \right) \times \mathbf{z}_l^{\text{Value}} \quad (\text{A4})$$

Forward projection may be applied to generate target values for each of  $\mathbf{z}_l^{\text{Query}}$ ,  $\mathbf{z}_l^{\text{Key}}$ ,  $\mathbf{z}_l^{\text{Value}}$ , using distinct data projection matrices  $\mathbf{Q}_l^{\text{Query}}$ ,  $\mathbf{Q}_l^{\text{Key}}$ ,  $\mathbf{Q}_l^{\text{Value}}$ , and a shared label projection matrix  $\mathbf{U}_l$ , such that for each patch, query matrix target potentials are given by

$$\tilde{\mathbf{z}}_{l,r}^{\text{Query}} = g_l \left( \mathbf{a}_{l-1,r} \mathbf{Q}_l^{\text{Query}} \right) + g_l \left( \mathbf{y} \mathbf{U}_l \right). \quad (\text{A5})$$

Thus, the query weight matrix is given by the penalised regression solution. Weights were fitted such that

$$\mathbf{W}_l^{\text{Query}} := \left( \sum_{r=1}^R \mathbf{A}_{l-1,r}^T \mathbf{A}_{l-1,r} + \lambda \mathbf{I} \right)^{-1} \left( \sum_{r=1}^R \mathbf{A}_{l-1,r}^T \tilde{\mathbf{Z}}_{l,r}^{\text{Query}} \right). \quad (\text{A6})$$

$\mathbf{W}_l^{\text{Key}}$  and  $\mathbf{W}_l^{\text{Value}}$ , are fitted in the same manner - using  $\mathbf{Q}_l^{\text{Key}}$  and  $\mathbf{Q}_l^{\text{Value}}$ , respectively, in place of  $\mathbf{Q}_l^{\text{Query}}$  in (A5).

#### A.4 Implementation of local learning methods

Local Supervision was implemented by generating auxiliary predictions  $\hat{\mathbf{y}}_1, \dots, \hat{\mathbf{y}}_{L-1}$  from a set of fixed linear operators  $\mathbf{U}_1, \dots, \mathbf{U}_{L-1}$  such that  $\hat{\mathbf{y}}_l = f_L(\mathbf{a}_l \mathbf{U}_l)$ . In each layer,  $\mathbf{W}_l$  was optimised to minimise the auxiliary loss  $\mathcal{L}_\uparrow(\hat{\mathbf{y}}_l, \mathbf{y})$  via gradient descent with two layers of backpropagation, such that

$$\nabla_{\mathbf{W}_l} \mathcal{L}_l = f'_l(\mathbf{U}_l^T) \cdot f'_L(\nabla_{\hat{\mathbf{y}}_l} \mathcal{L}_l) \cdot \mathbf{a}_{l-1}^T. \quad (\text{A7})$$

Here  $f'_l$  denotes the derivative of  $f_l$ . Local Supervision was implemented on convolutional layers by applying global-average pooling to generate a single vector representing mean neuronal activity over all convolutional windows, such that

$$\hat{\mathbf{y}}_l = \frac{1}{RC} \left( \sum_{r=1}^R \sum_{c=1}^C \mathbf{a}_{l-1,r,c}^T \mathbf{a}_{l-1,r,c} \right) \mathbf{U}_l. \quad (\text{A8})$$

The Forward-Forward algorithm was implemented by generating both “positive” data-label pairs  $[x, y]$  and “negative” data pairs  $[x, \check{y}]$  by concatenation. Positive activations were generated such that

$$\mathbf{a}_l = f_l(\mathbf{W}_l \dots f_1(\mathbf{W}_1[\mathbf{x}, \mathbf{y}]) \dots). \quad (\text{A9})$$

Negative activations were generated with spurious labels  $\check{y} \neq y$  such that

$$\check{\mathbf{a}}_l = f_l(\mathbf{W}_l \dots f_1(\mathbf{W}_1[\mathbf{x}, \check{\mathbf{y}}]) \dots). \quad (\text{A10})$$

Thus, local auxiliary loss functions were computed using threshold hyperparameter  $\theta = 2$  and logistic sigmoid function  $\sigma$ , computing auxiliary loss  $\mathcal{L}_l$  the such that

$$\mathcal{L}_l := \sigma(\|\check{\mathbf{a}}_l\|_2^2 - \theta) + \sigma(\theta - \|\mathbf{a}_l\|_2^2). \quad (\text{A11})$$

In MLP implementations, concatenation was implemented with supplementary input neurons to hold the label information as a one-hot vector. In convolutional implementations, the label was concatenated in the channel dimension, such that each channel indicated a single class, with a constant value over all kernel positions. Predictive Coding [5, 8] was implemented using inverse layers  $\mathbf{W}_l^{\text{Back}} \in \mathbb{R}^{m_l \times m_{l-1}}$  for each weight matrix  $\mathbf{W}_l$ , to estimate the pre-synaptic inputs from the post-synaptic outputs, such that

$$\hat{\mathbf{a}}_{l-1} := f_l^{\text{Back}} \left( \mathbf{a}_l \mathbf{W}_l^{\text{Back}} \right) \quad (\text{A12})$$

The local loss is given by the reconstruction error

$$\mathcal{L}_l := \|\mathbf{a}_{l-1} - \hat{\mathbf{a}}_{l-1}\|_2^2 \quad (\text{A13})$$

Similarly, Difference Target Propagation [1] aims to reconstruct presynaptic inputs, such that

$$\hat{\mathbf{a}}_{l-1} := \mathbf{a}_{l-1} - f_l^{\text{Back}}(\mathbf{a}_l \mathbf{W}_l^{\text{Back}}) + f_l^{\text{Back}}(\hat{\mathbf{a}}_l \mathbf{W}_l^{\text{Back}}) \quad (\text{A14})$$

In our implementations, we set  $f_l^{\text{Back}} = \text{ReLU}$  in both Predictive Coding and Difference Target Propagation models.

## A.5 Analysis of label projection approaches

We now consider the necessity of pre-synaptic input projections, which distinguish Forward Projection from alternative feedback-free approaches such as simple label projection and noisy label projection. The objective is to generate a weight matrix  $\mathbf{W}_l \in \mathbb{R}^{m_{l-1} \times m_l}$ , given pre-synaptic inputs,  $\mathbf{A}_{l-1} \in \mathbb{R}^{N \times m_{l-1}}$ , and label matrix  $\mathbf{Y} \in \mathbb{R}^{N \times m_L}$ . As described previously, given some target potentials  $\tilde{\mathbf{Z}}$ , weights will be fitted by equation (2), such that

$$\mathbf{W}_l = (\mathbf{A}_{l-1}^T \mathbf{A}_{l-1} + \lambda \mathbf{I})^{-1} \mathbf{A}_{l-1}^T \tilde{\mathbf{Z}}. \quad (\text{A15})$$

We let  $\text{rank}(\tilde{\mathbf{Z}})$  denote the column rank of  $\tilde{\mathbf{Z}}$  – the maximum number of linearly independent column vectors in its column space. Since  $\mathbf{W}_l$  is a linear function of  $\tilde{\mathbf{Z}}$ , we have  $\text{rank}(\mathbf{W}_l) \leq \text{rank}(\tilde{\mathbf{Z}})$ .

We first consider target generation by simple label projection, such that  $\tilde{\mathbf{Z}}_l := \mathbf{Y} \mathbf{U}_l$ . Here we have  $\text{rank}(\tilde{\mathbf{Z}}) \leq \text{rank}(\mathbf{Y}) \leq m_L$ . Where  $m_l \gg m_L$ , this implies severe degeneracy of  $\mathbf{W}_l$ , predisposing to correlated or redundant neuronal activities in  $\mathbf{A}_l$ . We next consider target generation by noisy label projection, using random Gaussian noise matrix  $\mathbf{E} \in \mathbb{R}^{N \times m_l}$  to perturb targets such that  $\tilde{\mathbf{Z}}_l := \mathbf{Y} \mathbf{U}_l + \mathbf{E}$ . In this case, we have  $\text{rank}(\tilde{\mathbf{Z}}_l) \leq \text{rank}(\mathbf{E}) \leq m_l$ . However, as  $\mathbf{E}$  is random and independent of  $\mathbf{Y}$ , this perturbation strategy may adversely affect label modelling of  $\mathbf{Y}$ . By adding projections of label and pre-synaptic inputs, such that  $\tilde{\mathbf{Z}}_l := \mathbf{a}_{l-1} \mathbf{Q}_l + \mathbf{Y} \mathbf{U}_l$ , we improve the upper bound to

$$\text{rank}(\tilde{\mathbf{Z}}_l) \leq \text{rank}(\mathbf{A}_{l-1}) + \text{rank}(\mathbf{Y}) \leq m_{l-1} + m_L, \quad (\text{A16})$$

without fitting  $\mathbf{W}_l$  to noise. Accordingly, the targets generated by our proposed method  $\tilde{\mathbf{Z}}_l := g_l(\mathbf{a}_{l-1} \mathbf{Q}_l) + g_l(\mathbf{Y} \mathbf{U}_l)$  are subject to the same upper bound  $\text{rank}(\tilde{\mathbf{Z}}_l) \leq (m_{l-1} + m_L)$ .

## A.6 Computing the Forward Projection estimator

Neural network models often manage storage demands by utilizing data mini-batches, allowing them to train on arbitrarily large datasets without a corresponding increase in memory requirements. Although the Forward Projection estimator described in equation (2) includes large matrix terms  $\mathbf{A} \in \mathbb{R}^{n \times m_{l-1}}$  and  $\mathbf{Z} \in \mathbb{R}^{n \times m_{l-1}}$ , these do not need to be loaded into memory. Assume  $\mathbf{A}_{l-1} \in \mathbb{R}^{N \times m_{l-1}}$  and  $\mathbf{Y} \in \mathbb{R}^{N \times m_L}$  are available as a set of row-vectors  $\{\mathbf{a}_{i,l-1}\}_{i=1}^N \subset \mathbb{R}^{1 \times m_{l-1}}$ . and  $\{\mathbf{y}_i\}_{i=1}^N \subset \mathbb{R}^{1 \times m_L}$ . The

matrix cross product is the sum of the row outer products, such that

$$\mathbf{A}_{l-1}^T \mathbf{A}_{l-1} = \sum_{i=1}^N \mathbf{a}_{i,l-1} \mathbf{a}_{i,l-1}^T. \quad (\text{A17})$$

Therefore, the  $\mathbf{A}_{l-1}^T \mathbf{A}_{l-1} \in \mathbb{R}^{m_{l-1} \times m_{l-1}}$  term may be accumulated sequentially over instances  $\{\mathbf{a}_{1,l-1}, \dots, \mathbf{a}_{N,l-1}\}$ , with  $\mathcal{O}(m_{l-1}^2)$  memory and  $\mathcal{O}(Nm_{l-1}^2)$  compute, such that

$$(\mathbf{A}_{l-1}^T \mathbf{A}_{l-1})^{(i)} = (\mathbf{A}_{l-1}^T \mathbf{A}_{l-1})^{(i-1)} + \mathbf{a}_{i,l-1} \mathbf{a}_{i,l-1}^T, \quad (\text{A18})$$

where  $(\mathbf{A}_{l-1}^T \mathbf{A}_{l-1})^{(0)}$  is zero matrix of dimension  $m_{l-1} \times m_{l-1}$ . Assume  $\mathbf{Y} \in \mathbb{R}^{N \times m_L}$  is available as  $\{\mathbf{y}_i\}_{i=1}^N \subset \mathbb{R}^{1 \times m_L}$ . We may generate the corresponding target potentials  $\{\tilde{\mathbf{z}}_{i,l-1}\}_{i=1}^N \subset \mathbb{R}^{1 \times m_l}$ , using predetermined matrices  $\mathbf{Q}_l \in \mathbb{R}^{m_{l-1} \times m_l}$  and  $\mathbf{U}_l \in \mathbb{R}^{m_L \times m_l}$  according to (1). Thus,  $\mathbf{A}_{l-1}^T \tilde{\mathbf{z}}_l \in \mathbb{R}^{m_{l-1} \times m_l}$  may also be accumulated sequentially such that

$$\mathbf{A}_{l-1}^T \tilde{\mathbf{z}}_l = \sum_{i=1}^N \mathbf{a}_{i,l-1} \tilde{\mathbf{z}}_{i,l-1}^T, \quad (\text{A19})$$

requiring  $\mathcal{O}(m_{l-1} m_l)$  memory and  $\mathcal{O}(Nm_{l-1} m_l)$  compute. Following sequential computation of equations (A18) and (A19), equation (A20) may be computed with one order  $\mathcal{O}(m_{l-1}^3)$  matrix inversion and one order  $\mathcal{O}(m_{l-1}^2 m_l)$  matrix multiplication, yielding:

$$\mathbf{W}_l = (\mathbf{A}_{l-1}^T \mathbf{A}_{l-1} + \lambda \mathbf{I})^{-1} (\mathbf{A}_{l-1}^T \tilde{\mathbf{z}}_l). \quad (\text{A20})$$

## A.7 Information Encoding and Interpretability

We now consider the information encoding properties of Forward Projection training. Assuming  $g_l^{-1}$  exists everywhere, equation (1) relates labels  $\mathbf{y} \in \mathbb{R}^{1 \times m_L}$  to target potentials  $\tilde{\mathbf{z}}_l \in \mathbb{R}^{1 \times m_l}$ , given presynaptic inputs  $\mathbf{a}_{l-1} \in \mathbb{R}^{1 \times m_{l-1}}$  via projection matrices  $\mathbf{Q}_l \in \mathbb{R}^{m_{l-1} \times m_l}$  and  $\mathbf{U}_l \in \mathbb{R}^{m_L \times m_l}$ , such that

$$\mathbf{y} \mathbf{U}_l = g_l^{-1} (\tilde{\mathbf{z}}_l - g_l(\mathbf{a}_{l-1} \mathbf{Q}_l)). \quad (\text{A21})$$

Letting  $\mathbf{U}_l^+$  denote the Moore-Penrose inverse, and assuming that  $\mathbf{U}_l \mathbf{U}_l^+ \approx \mathbf{I}$ , we may reconstruct  $\mathbf{y}$ , such that

$$\mathbf{y} \approx g_l^{-1} (\tilde{\mathbf{z}}_l - g_l(\mathbf{a}_{l-1} \mathbf{Q}_l)) \mathbf{U}_l^+. \quad (\text{A22})$$

Assuming realised neuron pre-activation potentials  $\mathbf{z}_l$  are a good approximation of the target potentials, i.e.,  $\mathbf{z}_l \approx \tilde{\mathbf{z}}_l$ , we may estimate the label from the hidden layer, such that

$$\hat{\mathbf{y}}_l := g_l^{-1} (\mathbf{z}_l - g_l(\mathbf{a}_{l-1} \mathbf{Q}_l)) \mathbf{U}_l^+. \quad (\text{A23})$$

Thus, neural potentials are interpretable layer-wise as label predictions. Likewise, pre-synaptic inputs may be estimated such that

$$\hat{\mathbf{a}}_{l-1} := g_l^{-1} (\mathbf{z}_l - g_l(\hat{\mathbf{y}}_l \mathbf{U}_l)) \mathbf{Q}_l^+. \quad (\text{A24})$$

Thus, pre-synaptic inputs are encoded in a lossy manner in each layer’s neural pre-activation potentials. In our experiments, we employed the sign function for target generation, defined as:

$$g_l := \text{sign}(x) = \begin{cases} -1 & x < 0 \\ 0 & x = 0 \\ 1 & x > 0 \end{cases} \quad (\text{A25})$$

The function  $g_l := \text{sign}(x)$  was selected due to computational simplicity and predictable distribution. The tanh function was employed as a surrogate approximation for  $g_l^{-1}$ , yielding satisfactory results.

## A.8 Stability Experiments

Technical analysis and stability experiments were performed on MLP models training on the FMNIST data. The stability of layer explanations, on models fitted to different data folds, with different random projection matrices, using a  $4 \times 1000$  neuron feed-forward architecture was evaluated. Test performance of layer explanations improved progressively from the first layer to the final layer with low variability throughout (Figure A2-A). Model stability with respect to choices of the FP penalty parameter  $\lambda$  (Equation 2) in hidden layers was evaluated in a  $3 \times 1000$  neuron MLP. Test accuracies were stable from  $\lambda = 1.25$  to  $\lambda = 80$  with the highest observed performance at  $\lambda = 80$  (Figure A2-B). The mean variance of pixels in the FMNIST training dataset is  $\sigma_{\text{input}} = 0.087$ . Although additive gaussian noise caused progressive deterioration in model performance from  $\sigma_{\text{noise}} = 0.1$  to  $\sigma_{\text{noise}} = 1$ , test accuracy remained above 0.819 for all  $\sigma_{\text{noise}} < 0.4$ , which corresponds to a signal-to-noise ratio of approximately 1 : 4.6 (Figure A2-C). The impact of the randomised projections on model performance was assessed in 3-layer MLP models with  $2 \times 1000$  hidden neurons in the first two layers and  $m_3 \in \{250, 500, 1000\}$  in the penultimate layer, with stable test performance observed throughout (Figure A2-D).

## A.9 Optimisation Theory

We now compare the fit of the Forward Projection estimator in a two-layer network, to that of a simple linear estimator in random data. We consider a dataset  $\{\mathbf{x}_i, \mathbf{y}_i\}_{i=1}^N$  with random Gaussian distribution such that  $\mathbf{x}_i \in \mathcal{N}(\mathbf{0}, \mathbf{I}_m)$  and an independent random normal target  $\mathbf{y}_i \in \mathcal{N}(\mathbf{0}, \mathbf{I}_d)$ . We assume  $N > m > d$ . We consider a fully connected neural network with a single hidden layer of dimension  $m$ , with relu-activation. The task is to identify network weights  $\{\mathbf{W}_1, \mathbf{W}_2\}$  to minimise the error  $\|\mathbf{Y} - \text{ReLU}(\mathbf{X}\mathbf{W}_1)\mathbf{W}_2\|$ . We first consider the expected error of a single layer, linear model. For convenience, we will set the penalty factor  $\lambda = 0$ , such that

$$\mathbf{W}_1 := (\mathbf{X}^T \mathbf{X})^{-1} \mathbf{X}^T \mathbf{Y}. \quad (\text{A26})$$

We denote the projection matrix of  $\mathbf{X}$  as

$$\mathbf{P}_x = \mathbf{X}(\mathbf{X}^T \mathbf{X})^{-1} \mathbf{X}^T. \quad (\text{A27})$$

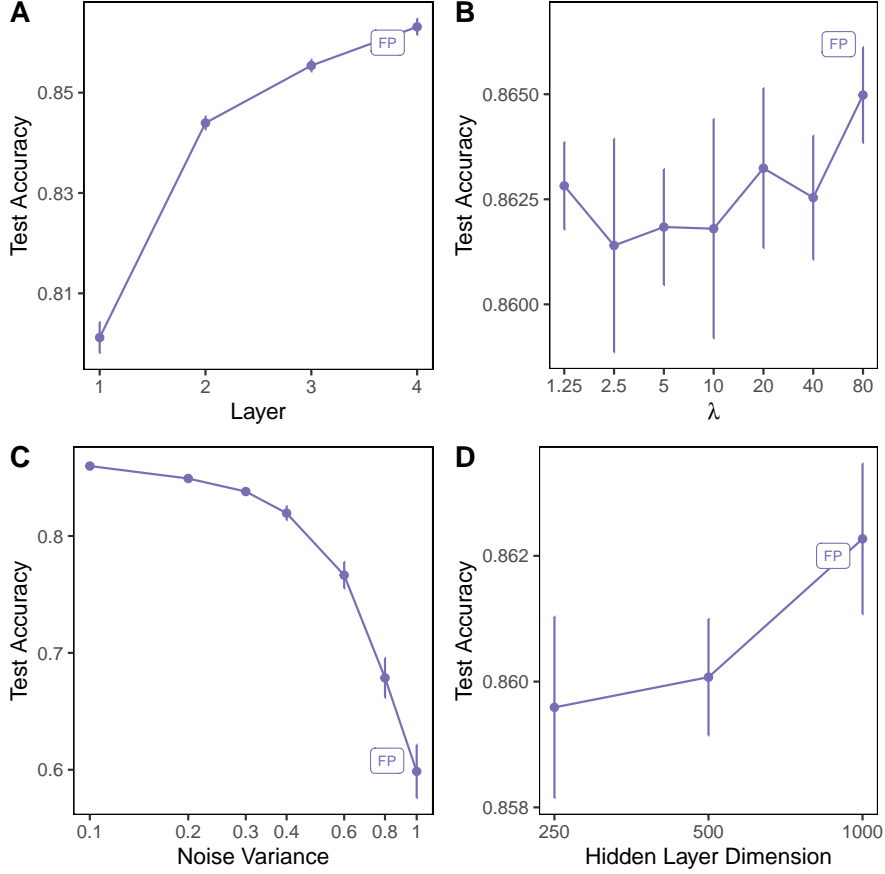


**Fig. A2:** A: Test accuracy of hidden layer explanations in a  $4 \times 1000$  neuron MLP trained by FP on FMNIST. B: Test accuracy of  $3 \times 1000$  neuron MLP trained by FP on FMNIST using different  $\lambda$  regularisation values. C: Test accuracy of  $3 \times 1000$  neuron MLP trained by FP on FMNIST with additive Gaussian noise in training data. D: Variability of FP training performance using different random projections in  $3 \times 1000$  neuron MLP on FMNIST. Points represent mean over all replicates and error bars represent  $\pm$  one standard deviation. BP: backpropagation; DTP: Difference Target Propagation; FF: Forward-Forward; FP: Forward Projection; LP: label projection; LPN: noisy label projection; LS: Local Supervision; PC: Predictive Coding; RF: random features.

Therefore, the spectrum of  $\mathbf{P}_{\mathbf{x}}$  is composed of a unit eigenvalue with multiplicity  $m$  and a zero eigenvalue with multiplicity  $N - m$ . Letting  $\hat{\mathbf{Y}}_1 = \mathbf{P}_{\mathbf{x}}\mathbf{Y}$ , we measure the error  $\mathbf{E}_1 = \mathbf{Y} - \mathbf{P}_{\mathbf{x}}\mathbf{Y}$ , such that

$$\|\mathbf{E}_1\| = \|(\mathbf{I} - \mathbf{P}_{\mathbf{x}})\mathbf{Y}\|. \quad (\text{A28})$$

The idempotent matrix  $(\mathbf{I} - \mathbf{P}_x)$  has rank  $N - m$ , as it is a projection matrix onto the orthogonal complement of the column space of  $\mathbf{X}$ . Therefore, the expected squared Frobenius norm of the error is given by

$$\mathbb{E} \left[ \frac{\|\mathbf{E}_1\|_F^2}{\|\mathbf{Y}\|_F^2} \right] = \frac{N - m}{N}. \quad (\text{A29})$$

Let  $\mathbf{U} \in \mathbb{R}^{d \times m}$  and  $\mathbf{Q} \in \mathbb{R}^{m \times m}$ . Letting  $\tilde{\mathbf{Z}} = \mathbf{XQ} + \mathbf{YU}$ , we now fit  $\mathbf{W}_1$  to estimate  $\tilde{\mathbf{Z}}$  from  $\mathbf{X}$ , such that

$$\mathbf{W}_1 := (\mathbf{X}^T \mathbf{X})^{-1} \mathbf{X}^T (\mathbf{XQ} + \mathbf{YU}). \quad (\text{A30})$$

As  $(\mathbf{X}^T \mathbf{X})^{-1} \mathbf{X}^T \mathbf{X} = \mathbf{I}$ , we have

$$\mathbf{W}_1 = \mathbf{Q} + (\mathbf{X}^T \mathbf{X})^{-1} \mathbf{X}^T \mathbf{YU}. \quad (\text{A31})$$

Thus, the pre-activation potential at the first layer is given by:

$$\mathbf{XW}_1 = \mathbf{XQ} + \mathbf{P}_x \mathbf{YU}. \quad (\text{A32})$$

Assuming  $\mathbf{U}$  has full row rank, we have  $\mathbf{U}\mathbf{U}^+ = \mathbf{I}_d$ , as  $m > d$ . Furthermore, As  $\mathbf{Q}$  and  $\mathbf{U}$  have random Gaussian entries, we have

$$\mathbb{E}[\mathbf{XW}_1 \mathbf{U}^+] = \mathbb{E}[\mathbf{XQ}\mathbf{U}^+] + \mathbb{E}[\mathbf{P}_x \mathbf{Y}\mathbf{U}\mathbf{U}^+] = \mathbf{P}_x \mathbf{Y} = \frac{1}{2} \hat{\mathbf{Y}}_1. \quad (\text{A33})$$

We now consider the covariance  $\text{Cov}(\mathbf{XW}_1, \mathbf{Y})$ . We assume  $\mathbf{XW}_1$  has zero mean. We have

$$\mathbb{E}[\langle \mathbf{XW}_1, \mathbf{Y} \rangle] = \mathbb{E}[\text{tr}((\mathbf{XQ} + \mathbf{P}_x \mathbf{YU})^T \mathbf{Y})] \quad (\text{A34})$$

By independence of  $\mathbf{Q}$ , we have  $\mathbb{E}[\text{tr}((\mathbf{XQ})^T \mathbf{Y})] = 0$ . The second term expands to

$$\text{tr}((\mathbf{P}_x \mathbf{YU})^T \mathbf{Y}) = \text{tr}(\mathbf{U}^T \mathbf{Y}^T \mathbf{P}_x \mathbf{Y}) \quad (\text{A35})$$

As  $\mathbf{P}_x$  is a projector matrix with rank  $m$ , and  $\mathbf{Y}$  is Gaussian, we have

$$\mathbb{E}[\mathbf{Y}^T \mathbf{P}_x \mathbf{Y}] = d \cdot \text{tr}(\mathbf{P}_x) \mathbf{I}_d = dm \cdot \mathbf{I}_d \quad (\text{A36})$$

Therefore

$$\mathbb{E}[\langle \mathbf{XW}_1, \mathbf{Y} \rangle] = \text{tr}(\mathbf{U}^T \mathbf{Y}^T \mathbf{P}_x \mathbf{Y}) = dm \cdot \text{tr}(\mathbf{U}^T) \quad (\text{A37})$$

As  $m > d$  and  $\mathbf{U}$  has random Gaussian entries, we have  $\text{Var}[\text{tr}(\mathbf{U}^T)] = d$ . Therefore, we have

$$\mathbb{E}[|\langle \mathbf{XW}_1, \mathbf{Y} \rangle|] = |\text{tr}(\mathbf{U}^T \mathbf{Y}^T \mathbf{P}_x \mathbf{Y})| \sim dm\sqrt{d}. \quad (\text{A38})$$

After normalising for  $\|\mathbf{XW}_1\|_F \|\mathbf{Y}\|_F \sim \sqrt{Nm} \cdot \sqrt{Nd}$ , the correlation magnitude scales according to

$$\mathbb{E}[|\text{Corr}(\mathbf{XW}_1, \mathbf{Y})|] \sim \frac{\text{tr}(\mathbf{XW}_1, \mathbf{Y})}{\|\mathbf{XW}_1\|_F \|\mathbf{Y}\|_F} = \frac{d\sqrt{m}}{N}. \quad (\text{A39})$$

Assuming  $\text{rank}(\mathbf{A}) = m$ , we may define  $\mathbf{P}_a = \mathbf{A}(\mathbf{A}^T \mathbf{A})^{-1} \mathbf{A}^T$ . We note that  $\mathbf{A}$  is dependent on  $\mathbf{Y}$  with a non-linear relationship, which is induced by the ReLU activations. We now consider modelling  $\mathbf{Y}$  in  $\mathcal{C}(\mathbf{A}) \cap \mathcal{C}(\mathbf{X})^\perp$ , the subspace of  $\mathbf{A}$  orthogonal to  $\mathbf{X}$ . For large  $N$ , application of ReLU nonlinearities in the construction of  $\mathbf{A}$  may yield  $\dim(\mathcal{C}(\mathbf{A}) \cap \mathcal{C}(\mathbf{X})^\perp) \approx m$ . Recall from (A39) that the column space of  $\mathbf{XW}_1$  is correlated with  $\mathbf{Y}$ . As  $\mathbf{A} = \text{ReLU}(\mathbf{XW}_1)$ , the column space of  $\mathbf{A}$  remains correlated with  $\mathbf{Y}$ . Therefore

$$\mathbb{E} \left[ \frac{\|\mathbf{Y} - \mathbf{P}_a \mathbf{Y}\|_F^2}{\|\mathbf{Y}\|_F^2} \right] < \frac{N - m}{N} \quad (\text{A40})$$

Therefore, even when modelling pure Gaussian noise, the error of the two-layer model is lower than that of the simple linear predictor.

## A.10 Modelling high dimensional labels

From (A23), we have:

$$\hat{\mathbf{y}}_l := g_l^{-1}(\mathbf{z}_l - g_l(\mathbf{a}_{l-1} \mathbf{Q}_l)) \mathbf{U}_l^+. \quad (\text{A41})$$

For simplicity, we analyse the special case that  $g_l$  is the identity function yielding,

$$\hat{\mathbf{y}}_l := (\mathbf{z}_l - \mathbf{a}_{l-1} \mathbf{Q}_l) \mathbf{U}_l^+. \quad (\text{A42})$$

Recalling that the realised potentials are estimates of pre-defined target potentials, such that  $\mathbf{z}_l = \tilde{\mathbf{z}}_l - \mathbf{e}_l$ , we have

$$\hat{\mathbf{y}}_l := (\tilde{\mathbf{z}}_l - \mathbf{e}_l - \mathbf{a}_{l-1} \mathbf{Q}_l) \mathbf{U}_l^+. \quad (\text{A43})$$

Applying the identity function as  $g_l$  in equation (1), we have

$$\tilde{\mathbf{z}}_l = \mathbf{a}_{l-1} \mathbf{Q}_l + \mathbf{y} \mathbf{U}_l. \quad (\text{A44})$$

Substituting, we have

$$\hat{\mathbf{y}}_l = (\mathbf{y} \mathbf{U}_l - \mathbf{e}_l) \mathbf{U}_l^+. \quad (\text{A45})$$

Assuming, that  $\mathbf{U}$  has full row rank, and that  $m_l > m_L$ , we have  $\mathbf{U}_l \mathbf{U}_l^+ = \mathbf{I}_{m_L}$ . Therefore

$$\hat{\mathbf{y}}_l = \mathbf{y} - \mathbf{e}_l \mathbf{U}_l^+. \quad (\text{A46})$$

Assuming  $\mathbf{e}_l \sim \mathcal{N}(0, \epsilon \mathbf{I}_{m_l})$  for some  $\epsilon \in \mathbb{R}$ , we have  $\mathbb{E}[\mathbf{e}_l \mathbf{U}_l^+] = 0$ , as  $\mathbf{U}$  is random and independent of  $\mathbf{e}_l$ . Therefore

$$\mathbb{E}[\hat{\mathbf{y}}_l] = \mathbf{y} - \mathbb{E}[\mathbf{e}_l \mathbf{U}_l^+] = \mathbf{y}. \quad (\text{A47})$$

Therefore  $\text{Var}[\tilde{\mathbf{y}}_l - \mathbf{y}_l] = \text{Var}[\mathbf{e}_l \mathbf{U}_l^+]$ . Using the property of linear transformation of Gaussian variables, we have

$$\text{Var}[\mathbf{e}_l \mathbf{U}_l^+] = \epsilon \mathbf{U}_l^+ (\mathbf{U}_l^+)^T. \quad (\text{A48})$$

We note that

$$\text{Tr} \left( \mathbf{U}_l^+ (\mathbf{U}_l^+)^T \right) = \|\mathbf{U}_l^+\|_F^2 \quad (\text{A49})$$

Furthermore, it is noted that

$$\mathbb{E} [\|\mathbf{U}_l^+\|_F^2] = \mathbb{E} \left[ \text{Tr} \left( \mathbf{U}_l^+ (\mathbf{U}_l^+)^T \right) \right] \approx \mathbb{E} [\text{Tr} \left( (\mathbf{U}_l \mathbf{U}_l^T)^{-1} \right)] \quad (\text{A50})$$

We observe that the Frobenius norm  $\|\mathbf{U}_l^+\|_F^2$  equals the sum of inverse squared singular values

$$\|\mathbf{U}_l^+\|_F^2 = \sum_{i=1}^{m_L} \frac{1}{\sigma_i^2}. \quad (\text{A51})$$

Selecting  $\mathbf{U}_l$  with independent and identically distributed Gaussian entries, the singular values squared are the eigenvalues of the Wishart matrix

$$\mathbf{U}_l \mathbf{U}_l^T \sim \mathcal{W}_{m_L}(m_l, \mathbf{I}_{m_l}). \quad (\text{A52})$$

Therefore we have  $\mathbb{E}[\text{Tr} \left( (\mathbf{U}_l \mathbf{U}_l^T)^{-1} \right)] = \frac{m_L}{m_l - m_L - 1}$  for  $m_L < m_l$ . Thus, the expectation  $\mathbb{E} \left[ \text{Tr} \left( \mathbf{U}_l^+ (\mathbf{U}_l^+)^T \right) \right]$  increases with  $m_L$  and decreases with  $m_l$ . Thus, higher dimensional labels are subject to poorer encoding, for a given hidden layer dimension. Conversely, for a given label dimension, it is expected that representation and learning will improve with increases of the hidden layer dimension. Accordingly, adequate modelling of high dimensional labels may require larger hidden layer dimensions.

### A.11 Modelling with Challenging Hidden Activation Functions

Neural networks commonly employ simple activation functions such as ReLU, due to low computational complexity and favourable approximation properties. Alternative hidden activation functions in sigmoid, polynomial and modulo families are desirable for modelling various physical and theoretical systems [40]. However, problems such as gradient vanishing and saturation may arise when these activation functions are trained via SGD-based methods [40, 41]. SGD-based training is not directly applicable where  $f_l$  is undifferentiable, necessitating the use of surrogate gradient methods. Many undifferentiable activation functions, such as the Heaviside step function, have attractive properties of low computational complexity and biological plausibility. Forward propagation does not require hidden activation functions to be differentiable, as target potentials  $\tilde{\mathbf{Z}}_1, \dots, \tilde{\mathbf{Z}}_{l-1}$  are modelled before activation. Thus, Forward Projection presents many opportunities for modelling activation functions for which SGD-based training is intractable. Going beyond the standard activation functions, we evaluated the performance of functions which present a challenge for SGD-based training. Networks were modelled with modulo 2 activation (“mod2”:  $f(x) = x \bmod 2$ ) and “square” activation  $f(x) = x^2$ . To control the desired range for the target potentials, an additive constant  $\alpha \in \mathbb{R}$  was included in the target generation function, such that

$$\tilde{\mathbf{z}}_l = \text{sign}(\mathbf{a}_{l-1} \mathbf{Q}_l) + \text{sign}(\mathbf{y} \mathbf{U}_l) + \alpha. \quad (\text{A53})$$

Dataset	Method Activation	Forward projection (Ours)	Random features	Local Supervi- sion	Forward Forward	Backprop. (reference standard)
FMNIST	mod2	60.9 ± 0.4	34.4 ± 0.4	10.0 ± 0.2	9.8 ± 0.3	9.9 ± 0.2
	square	86.0 ± 0.3	67.0 ± 0.2	81.5 ± 1.4	38.6 ± 39.1	65.9 ± 6.2
Promoters	mod2	76.7 ± 0.4	49.7 ± 0.6	50.0 ± 0.0	50.2 ± 0.5	49.9 ± 0.2
	square	78.4 ± 6.2	50.0 ± 0.0	52.2 ± 3.0	54.4 ± 9.8	54.5 ± 5.7
PTBXL-MI	mod2	76.6 ± 2.5	50.0 ± 0.3	50.0 ± 0.0	48.5 ± 2.2	50.0 ± 0.0
	square	83.3 ± 1.5	50.0 ± 0.0	51.0 ± 2.0	64.6 ± 4.7	51.4 ± 1.6

**Table A1:** Test accuracies of local learning methods in FashionMNIST, Promoters and PTBXL-MI tasks, using modulo 2 (“mod2”) ( $f(x) = x \bmod 2$ ) and square ( $f(x) = x^2$ ) activation functions. FP: Forward Projection; LS: Local Supervision; FF: Forward-Forward; BP: Backpropagation

This hyperparameter was predefined as  $\alpha = 0.5$  for both mod2 and square implementations. Forward projection yielded consistent performance across various activation functions in each dataset. In contrast, attempts at SGD-based training failed to converge in each task. Performance of Forward Projection, random features, Local Supervision, Forward-Forward and backpropagation modelling with square and mod2 activations is provided in Supplementary Table A1.

## A.12 Few-shot modelling

Discrimination performance of Difference Target Propagation and Predictive Coding methods in few-shot learning tasks is plotted in Figure A3. Both methods proved uninformative for few-shot learning CXR (Figure A3-A), OCT (Figure A3-B), and CIFAR tasks (Figure A3-C).

Discrimination performance (AUC) of Forward Projection, random features, Local Supervision, Forward-Forward, Predictive Coding, Difference Target Propagation and and backpropagation in few-shot modelling tasks is provided in Supplementary Table A2.

## A.13 Training Times

Training times and epochs for each method, in full dataset modelling. FMNIST was modelled with a  $3 \times 1000$  neuron MLP network. Sequential datasets (PTBXL-MI and Promoters) were modelled by a 1d-CNN architecture of four convolutional blocks with  $32 \times 2^{l-1}$  filters in the  $l$ -th block. CIFAR modelling used a vision transformer architecture operating on image patches of dimension  $4 \times 4$ , with a sequential stack of four multi-headed attention layers, each having 8 heads, embedding dimension 64, and MLP dimension 64. All experiments were run on the Google Colab service using an NVIDIA T4 graphics processing unit.

Dataset		Method	FP (ours)	RF	LS	FF	PC	DTP	BP	AUC
Partition	$N_{\text{train}}$									
CXR	Train	N=5	100.0 ± 0.0	100.0 ± 0.0	50.7 ± 16.0	52.0 ± 9.5	51.0 ± 12.9	53.9 ± 12.7	72.5 ± 9.4	
		N=10	100.0 ± 0.0	100.0 ± 0.0	48.7 ± 12.7	48.8 ± 6.3	49.4 ± 9.9	53.8 ± 10.4	69.0 ± 8.1	
		N=15	100.0 ± 0.0	100.0 ± 0.0	55.2 ± 13.9	51.1 ± 6.1	49.4 ± 9.5	50.4 ± 8.8	72.4 ± 10.6	
		N=20	100.0 ± 0.0	100.0 ± 0.2	58.5 ± 12.8	50.0 ± 5.5	50.2 ± 9.6	52.0 ± 7.4	72.6 ± 8.0	
		N=30	100.0 ± 0.0	99.9 ± 0.4	59.8 ± 15.5	50.0 ± 5.7	52.4 ± 9.0	49.4 ± 8.4	71.8 ± 9.6	
	N=40	100.0 ± 0.1	99.3 ± 0.8	61.4 ± 15.8	49.7 ± 4.8	52.1 ± 8.9	52.3 ± 7.9	74.3 ± 10.2		
	N=50	99.9 ± 0.2	98.4 ± 1.0	66.1 ± 14.8	49.4 ± 6.2	51.4 ± 8.2	52.2 ± 7.3	84.2 ± 9.8		
	Test	N=5	75.2 ± 7.0	67.6 ± 7.5	49.7 ± 8.8	49.3 ± 5.7	50.2 ± 8.1	51.8 ± 7.6	57.6 ± 7.6	
		N=10	76.6 ± 5.8	68.1 ± 6.0	47.9 ± 9.0	49.1 ± 5.7	49.3 ± 8.9	52.7 ± 8.3	59.7 ± 6.2	
		N=15	77.4 ± 4.5	69.2 ± 4.8	53.9 ± 12.3	49.9 ± 6.7	49.0 ± 8.3	50.2 ± 7.6	63.1 ± 8.6	
		N=20	78.9 ± 3.7	69.0 ± 4.9	58.9 ± 11.5	49.0 ± 5.8	49.6 ± 8.5	51.0 ± 7.1	66.1 ± 9.3	
		N=30	80.6 ± 3.7	69.5 ± 3.7	59.2 ± 14.0	51.2 ± 6.2	51.9 ± 8.8	49.1 ± 8.9	66.6 ± 8.0	
	N=40	81.7 ± 2.9	72.4 ± 3.7	61.2 ± 16.1	48.0 ± 6.4	50.3 ± 7.6	51.3 ± 8.6	70.2 ± 8.3		
	N=50	82.5 ± 3.5	72.2 ± 3.1	64.8 ± 14.9	49.4 ± 7.4	50.1 ± 7.9	50.9 ± 7.2	78.9 ± 8.3		
	OCT	Train	N=5	100.0 ± 0.0	100.0 ± 0.0	53.9 ± 27.2	49.4 ± 12.5	52.5 ± 23.0	56.9 ± 21.5	86.8 ± 13.2
N=10			100.0 ± 0.0	100.0 ± 0.0	58.3 ± 17.8	50.4 ± 12.2	51.4 ± 15.9	54.4 ± 13.8	83.3 ± 12.2	
N=15			100.0 ± 0.0	100.0 ± 0.0	57.1 ± 15.7	49.9 ± 11.2	49.6 ± 12.3	52.5 ± 13.8	80.5 ± 11.2	
N=20			100.0 ± 0.0	100.0 ± 0.0	53.4 ± 21.0	51.6 ± 9.8	52.9 ± 13.0	52.8 ± 11.7	88.9 ± 12.1	
N=30			100.0 ± 0.0	100.0 ± 0.0	58.0 ± 18.8	50.1 ± 11.3	50.1 ± 11.5	51.7 ± 9.7	83.7 ± 12.3	
N=40		100.0 ± 0.0	99.9 ± 0.3	61.4 ± 21.0	52.3 ± 9.2	52.2 ± 11.2	51.0 ± 12.6	88.0 ± 12.0		
N=50		100.0 ± 0.0	99.7 ± 0.7	61.7 ± 19.8	50.8 ± 13.6	51.1 ± 8.8	53.6 ± 11.0	95.2 ± 8.3		
Test		N=5	76.3 ± 11.5	63.1 ± 10.0	51.1 ± 17.6	52.5 ± 12.0	50.1 ± 15.6	47.1 ± 10.5	61.8 ± 17.4	
		N=10	84.5 ± 5.8	66.5 ± 7.7	54.6 ± 16.7	51.8 ± 12.1	49.0 ± 17.1	49.2 ± 11.6	71.8 ± 15.9	
		N=15	86.5 ± 7.8	68.7 ± 7.4	56.8 ± 16.3	47.8 ± 12.8	49.6 ± 13.6	52.2 ± 12.9	72.3 ± 14.4	
		N=20	88.4 ± 5.9	69.5 ± 6.0	49.6 ± 19.1	52.3 ± 13.0	50.2 ± 15.5	49.9 ± 14.7	82.4 ± 14.4	
		N=30	89.9 ± 4.0	70.5 ± 5.7	55.7 ± 20.9	51.8 ± 11.7	49.6 ± 15.5	48.4 ± 13.9	81.9 ± 12.1	
N=40		90.2 ± 5.0	73.3 ± 5.5	62.0 ± 25.1	50.6 ± 13.0	51.6 ± 16.5	51.1 ± 15.4	88.7 ± 9.3		
N=50		91.2 ± 4.7	73.6 ± 5.9	62.6 ± 23.8	49.7 ± 18.4	51.2 ± 12.9	51.2 ± 13.4	94.2 ± 6.6		
CIFAR		Train	N=25	95.3 ± 2.7	100.0 ± 0.0	71.6 ± 23.6	52.6 ± 9.7	49.6 ± 17.5	55.9 ± 16.2	96.8 ± 4.5
	N=50		96.0 ± 2.0	100.0 ± 0.0	78.9 ± 18.3	59.2 ± 21.0	60.3 ± 16.5	56.1 ± 13.8	99.4 ± 1.9	
	N=75		96.0 ± 1.6	100.0 ± 0.0	86.7 ± 5.2	67.5 ± 17.8	64.6 ± 15.1	63.4 ± 11.4	98.2 ± 2.5	
	N=100		95.9 ± 1.3	100.0 ± 0.1	88.7 ± 3.8	73.7 ± 10.6	69.6 ± 11.0	60.9 ± 8.9	99.9 ± 0.3	
	N=25		78.6 ± 3.4	78.6 ± 3.6	65.0 ± 20.5	52.5 ± 8.8	47.7 ± 14.6	54.2 ± 14.1	82.2 ± 2.4	
	N=50	83.1 ± 2.8	77.3 ± 3.1	74.2 ± 16.5	60.1 ± 22.8	58.5 ± 16.3	54.6 ± 13.4	86.3 ± 2.2		
	N=75	84.4 ± 1.7	76.2 ± 3.1	81.5 ± 2.6	68.3 ± 18.8	64.4 ± 15.0	62.8 ± 10.7	87.5 ± 2.1		
	N=100	86.1 ± 2.0	78.1 ± 2.6	83.5 ± 2.8	74.3 ± 9.7	68.6 ± 11.9	60.7 ± 9.4	89.5 ± 1.4		

**Table A2:** Train and Test AUC performance in few-shot learning experiments. AUC: area under curve. CXR: chest x-ray dataset. OCT: optical coherence tomography dataset. BP: Backpropagation; DTP: Difference Target Propagation; FF: Forward Forward; FP: Forward Projection; LS: Local Supervision; PC: Predictive Coding; RF: Random features

Dataset	Method Metric	FP	RF	LS	FF	PC	DTP	BP
FMNIST	Time (s)	0.3 ± 0.1	0.1 ± 0.0	46.9 ± 12.5	171.9 ± 56.6	150.2 ± 61.2	72.7 ± 26.4	22.4 ± 4.8
Promoters		6.5 ± 0.2	3.3 ± 0.6	91.6 ± 37.7	69.5 ± 12.4	258.9 ± 233.7	103.0 ± 23.6	30.9 ± 4.3
PTBXL-MI		10.6 ± 1.1	6.7 ± 0.8	56.3 ± 13.8	35.5 ± 11.9	73.3 ± 15.8	61.0 ± 24.2	18.7 ± 5.1
CIFAR	Epochs	16.3 ± 0.6	9.2 ± 0.6					43.3 ± 15.1
FMNIST		1.0 ± 0.0	1.0 ± 0.0	10.8 ± 3.6	40.2 ± 13.8	25.4 ± 10.2	13.6 ± 5.3	11.6 ± 2.7
Promoters		1.0 ± 0.0	1.0 ± 0.0	11.4 ± 4.9	6.2 ± 1.3	18.4 ± 17.5	7.8 ± 2.0	10.0 ± 1.4
PTBXL-MI		1.0 ± 0.0	1.0 ± 0.0	17.0 ± 4.3	7.2 ± 2.3	14.6 ± 3.3	13.8 ± 5.9	13.2 ± 3.6
CIFAR		1.0 ± 0.0	1.0 ± 0.0					10.8 ± 3.9

**Table A3:** Training times and epochs in full dataset modelling experiments. BP: Backpropagation; DTP: Difference Target Propagation; FF: Forward Forward; FP: Forward Projection; LS: Local Supervision; PC: Predictive Coding; RF: Random features

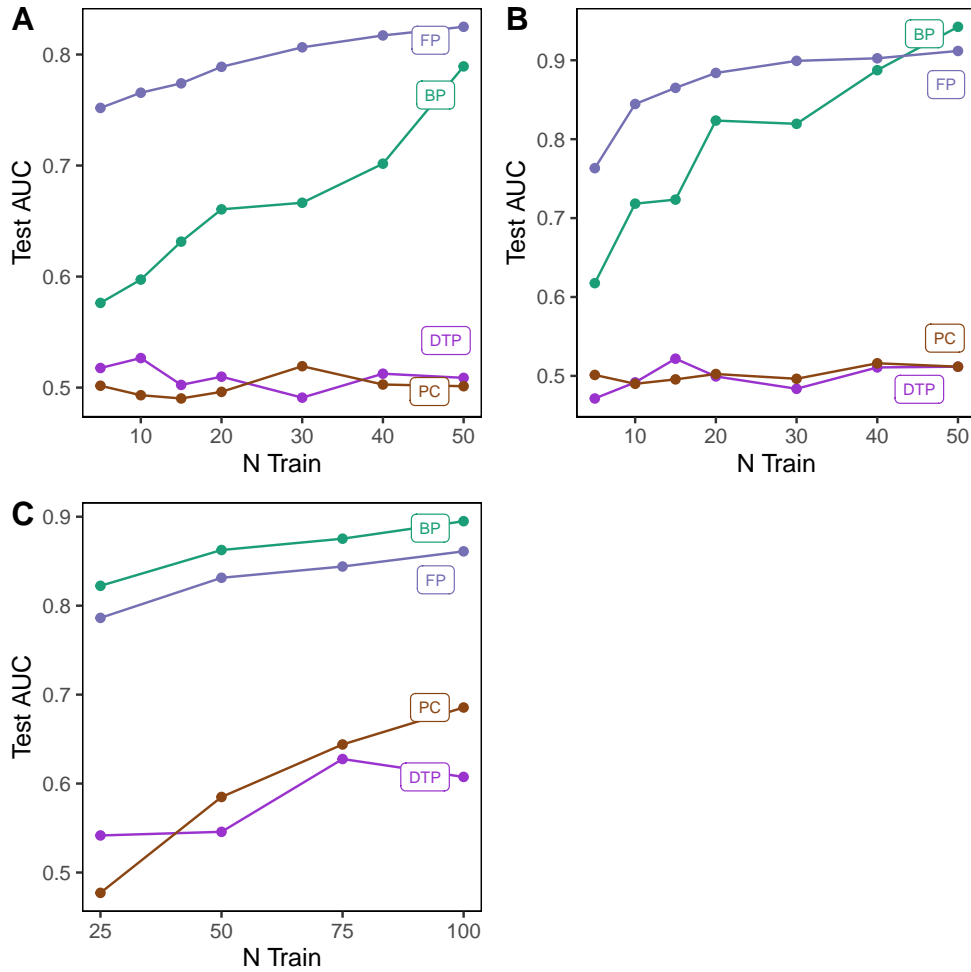


**Fig. A3:** Test performance of few-shot trained 2D-CNN models, showing Difference Target Propagation (DTP) and Predictive Coding (PC) methods. Mean test AUC is reported over 50 few-shot training experiments. A: Chest X-ray (CXR) task. B: Optical Coherence Tomography (OCT) task. C: CIFAR task in which models were required to classify the first two classes (aeroplane and automobile). Mean test AUC is reported over 50 few-shot training experiments. Models were fitted with  $N \in \{5, 10, 15, 20, 30, 40, 50\}$  training samples from each class in CXR and OCT tasks and  $N \in \{25, 50, 75, 100\}$  samples per class for the CIFAR task.